Bioactive Materials 44 (2025) 428–446

Contents lists available at ScienceDirect

Bioactive Materials

journal homepage: www.keaipublishing.com/en/journals/bioactive-materials

Targeted antimicrobial self-assembly peptide hydrogel with in situ bio-mimic remineralization for caries management

Li Zhou [a], Qing Liu [a], Zehui Fang [a], Quan Li Li [b,c,**], Hai Ming Wong [a,*]

[a] Faculty of Dentistry, The University of Hong Kong, Pokfulam Road, Hong Kong, 999077, China
[b] Institute of Oral Science, Department of Stomatology, Longgang Otorhinolaryngology Hospital, No. 3004L Longgang Avenue, Shenzhen, 518172, China
[c] Key Lab. of Oral Diseases Research of Anhui Province, College and Hospital of Stomatology, Anhui Medical University, Meishan Road, Hefei, 230000, China

ARTICLE INFO

Keywords:
Targeted antimicrobial therapy
Mineralization
Caries
Self-assembly hydrogel
Transcriptomic analysis
Molecular dynamics analysis

ABSTRACT

The single-function agents with wide-spectrum activity which tend to disturb the ecological balance of oral cavity cannot satisfy dental treatment need. A multi-functional agent with specifically targeted killing property and in situ remineralization is warranted for caries management. A novel multi-functional agent (8DSS-C8-P-113) consisting of three domains, i.e., a non-specific antimicrobial peptide (AMP) (P-113), a competence stimulating peptide (C8), and an enhancing remineralization domain (8DSS), is fabricated and evaluated in this study. The findings demonstrates that 2 μM mL^{-1} of 8DSS-C8-P-113 eliminates planktonic *Streptococcus mutans* (*S. mutans*) without disrupting the oral normal flora. At a concentration of 8 μM mL^{-1}, it exhibits the ability to prevent *S. mut*ans' adhesion. Furthermore, 8DSS-C8-P-113 self-assembles a hydrogel state at the higher concentration of 16 μM mL^{-1}. This hydrogel self-adheres on the tooth surface, resisting acid attack, eradicating *S. mutans'* biofilm, and inducing mineralization in order to facilitate the repair of demineralized dental hard tissue. Its significant effectiveness in reducing the severity of dental caries is also demonstrated in vivo in a rat model. This study suggests that the multi-functional bioactive AMP 8DSS-C8-P-113 is a promising agent to specifically target pathogen, prevent tooth demineralization, and effectively induce in situ bio-mimic remineralization for the management of dental caries.

1. Introduction

Antibiotics, a cornerstone of modern medicine, have a major role in the prevention and treatment of microbial infectious diseases [1]. However, the overuse of antibiotics and the resulting development of bacterial resistance has diminished the effectiveness of drugs, posing a threat to public health [2]. Antimicrobial peptides (AMPs) and proteins, a key component of innate immunity, have been recognized as potential antibiotic substitutes due to their potent antimicrobial activities and low bacterial resistance [3]. AMPs are found in the different species including human, mammals, amphibians, insects, microorganisms and plants, with different structures such as α-helix, β-sheet, and linear extension [4]. In the oral cavity, AMPs are expressed in the salivary glands, oral mucosa, bone marrow, and dental pulp to achieve immune activation, inflammation and wound healing [3]. AMPs also works with α-defensins, β-defensins, histatins, statherin, cathelicidin and adrenomedullin to maintain the dynamic balance between host and microbe [5]. Human AMPs usually exhibit broad spectrum activities against gram-positive and gram-negative bacteria, yeasts, fungi and viruses [6]. Nevertheless, wide-spectrum activity alters the ecological harmony of the natural microbiota leading to dysbiosis. Recently, AMPs that kill specific pathogens without affecting normal microbial flora have been investigated [7]. These specifically (or selectively) targeted antimicrobial peptides (STAMPs) consist of two functionally independent peptide components: a targeting region comprised of a high affinity binding peptide for recognizing bacteria, and a killing region comprised of a non-specific AMP for destroying bacteria [7,8].

Streptococcus mutans (*S. mutans*) is a facultatively anaerobic, gram-

Peer review under responsibility of KeAi Communications Co., Ltd.
* Corresponding author.
** Corresponding author. Institute of Oral Science, Department of Stomatology, Longgang Otorhinolaryngology Hospital, No. 3004L Longgang Avenue, Shenzhen, 518172, China.
E-mail addresses: hkupplily@gmail.com (L. Zhou), liuq1029@connect.hku.hk (Q. Liu), aydfangzehui@163.com (Z. Fang), ql-li@126.com (Q.L. Li), wonghmg@hku.hk (H.M. Wong).

https://doi.org/10.1016/j.bioactmat.2024.10.022
Received 15 August 2024; Received in revised form 1 October 2024; Accepted 20 October 2024

Table 1
Amino acid sequence and molecular weight of peptides.

Peptide	Amino acid sequence	Molecular wt
P-113	AKRHHGYKRKFH	1564.79
P-113-*DPS*	AKRHHGYKRKFH*SpSp*	1898.91
DPS-P-113	*SpSp*AKRHHGYKRKFH	1898.91
P-113-*8DSS*	AKRHHGYKRKFH*DSSDSSDSSDSSDSSDSSDSSDSS*	3878.73
8DSS-P-113	*DSSDSSDSSDSSDSSDSSDSSDSS*AKRHHGYKRKFH	3878.73
C8-P-113	**TFFRLFNR**AKRHHGYKRKFH	2647.05
C8-P-113-*DPS*	**TFFRLFNR**AKRHHGYKRKFH*SpSp*	Not be synthesized successfully
DPS-**C8**-P-113	*SpSp***TFFRLFNR**AKRHHGYKRKFH	2981.16
C8-P-113-*8DSS*	**TFFRLFNR**AKRHHGYKRKFH*DSSDSSDSSDSSDSSDSSDSSDSS*	4960.99
8DSS-**C8**-P-113	*DSSDSSDSSDSSDSSDSSDSSDSS***TFFRLFNR**AKRHHGYKRKFH	4960.99

positive coccus and has been identified as a primary causative factor of dental caries in humans [9]. *S. mutans* effectively colonizes onto tooth surface, utilizing dietary sucrose as an energy source, and fermenting carbohydrates such as glucose, fructose, sucrose, and lactose to produce lactic acid [10]. These acidic byproducts, with a pH below 5.5, erode the hydroxyapatite (HAP) crystal structure of the tooth, leading to dental caries. The progression of tooth decay into the dental pulp results in inflammation and pain, and can significantly impact essential functions such as eating, chewing, smiling and communication. Hence, the inhibition of *S. mutans* is crucial in preventing the occurrence of dental caries. There are many AMPs killing *S. mutans*, including human natural AMPs, such as LL37, hBD-2, hBD-3, HNP1, HNP2, HNP3 and Histatin 5; and synthetic, mimicked or modified natural AMPs, such as KR12-KAKE, hBD3-C15, dhvar 5 and P-113 [11]. These AMPs all have broad-spectrum activity. For instance, LL37 can kill *S. sobrinus, S. salivarius, S. sanguis* and *S. mitis* while killing *S. mutans* [12]. However, a STAMP consisting of a competence stimulating peptide (CSP) with 8 amino acids TFFRLFNR (C8) for targeting the ComD receptor of *S. mutans* and non-specific AMP G2 for destroying *S. mutans* can kill *S. mutans* without influencing other non-pathogenic species, such as *S. gordonii Challis* and *S. sanguinis* [13]. This species-specific targeting strategy protects oral normal flora effectively.

P-113 (AKRHHGYKRKFH) is a derivative of the human AMP Histatin 5. P-113 consists of 12 amino acids, and retains the antibacterial and antifungal activities of the parent molecule [14]. It has a broad antimicrobial spectrum against *Pseudomonas aeruginosa* (the major pathogenic bacteria of cystic fibrosis), *Staphylococcus* (the major pathogenic bacteria of most infections), *Candida albicans* (the major pathogenic fungus of candidiasis), and *S. mutans* (the major pathogenic bacteria of dental caries) [15–17]. We have designed and fabricated a bi-functional AMP, the P-113-DPS in our previous study [18]. The P-113 of it has the antibacterial activity for *S. mutans*, and two phosphoserines (DPS), bearing a negative charge that strongly attract Ca^{2+}, give it the improved remineralization ability on the acid-lesioned enamel surface [18]. Despite P-113 or P-113-DPS's ability to inhibit *S. mutans*, their broad-spectrum activity may cause potential harm to the normal oral flora. Based on the STAMP strategy, we planned to design a novel functional AMP with three components: a non-specific AMP (P-113), a specific targeting domain (C8), and an enhancing remineralization domain. DPS and 24 amino acids DSSDSSDSSDSSDSSDSSDSSDSS (8DSS) were selected as the candidates for enhancing remineralization [19,20]. Hence, four multi-functional AMPs were fabricated including C8-P-113-DPS, DPS-C8-P-113, C8-P-113-8DSS, and 8DSS-C8-P-113 in this study.

We firstly aimed to determine the optimal multi-functional AMP that possessed the best bioactive properties among C8-P-113-DPS, DPS-C8-P-113, C8-P-113-8DSS, and 8DSS-C8-P-113. The following bioactive properties were assessed: (1) anti-bacterial activity; (2) characterization of peptides; (3) the ability to promote remineralization; and (4) the ability to inhibit demineralization in the artificial caries model. Secondly, mechanistic studies were conducted and antimicrobial activity of the optimal multi-functional AMP was investigated by transcriptomic analysis. Thirdly, the optimal multi-functional AMP's activity to improve remineralization of was explored by molecular dynamics (MD) analysis. Finally, a rat caries model was established to evaluate the optimal multi-functional AMP's efficacy against dental caries and its biocompatibility.

2. Methods

2.1. Synthesis and purification of peptides

All peptides listed in Table 1 were synthesized (GL Biochem Ltd, Shanghai, China) using the standard 9-fluorenylmethoxycarbonyl (FMOC) solid-phase synthesis methods, and were purified (> 95 %) by reverse-phase High-Performance Liquid Chromatography (HPLC). Peptide molecular mass was characterized by Mass Spectrometry (MS). HPLC chromatograms at 220 nm and MS spectrum of peptides are shown in Fig. S1 and Fig. S2, respectively. Lyophilized peptides were stored at −70 °C and dissolved in 4-(2-hydroxyethyl)-1-piperazineeth anesulfonic acid (HEPES, 10 mM, pH = 7) buffer prior to use.

Highlighted three function domains: non-specific AMP domain underlined, specific targeting domain in bold, and enhancing remineralization domain in italic font, respectively.

2.2. Preparation of tooth slices

Human third molars were obtained from patients who provided written informed consent, and the study was approved by the Institutional Review Board of the University of Hong Kong/Hospital Authority Hong Kong West Cluster (IRB No: UW22-657). Tooth slices measuring 3 × 3 × 1.5 mm^3 (total number: 217) were prepared from the smooth surfaces of healthy teeth using a water-cooled diamond saw (IsoMet low-speed saw, Buehler, Lake Bluff, IL, USA). Micro Computed Tomography (MicroCT Skyscan 1172, Bruker, USA) was used to identify one working surface of complete enamel tissue from each tooth slice. The enamel working side of the tooth slice was polished with abrasive paper grit (ranging from 320 to 4000 in ascending order), and the other sides were marked with acid-proof nail polish. All tooth slices were cleaned and stored in deionized water at 4 °C.

2.3. Anti-bacterial ability of peptides

2.3.1. Anti-planktonic bacterial ability

S. mutans (ATCC 35668, ATCC, Manassas, USA), *S. gordonii* (ATCC 35105, ATCC, Manassas, USA), and *S. sanguinis* (ATCC 10556, ATCC, Manassas, USA) strains were cultured in brain-heart infusion broth (BHI, Difco Laboratories, Detroit, USA) at 37 °C under anaerobic conditions (85 % N_2, 10 % H_2, and 5 % CO_2). Bacteria were harvested by centrifugation (5000 rpm, 10 min), washed once with sodium phosphate-buffered saline (PBS, 10 mM, pH = 7.2), and resuspended in BHI at a concentration of 1 × 10^6 CFU mL^{-1}.

A series of two-fold dilutions of P-113, P-113-DPS, DPS-P-113, P-113-8DSS, 8DSS-P-113, C8-P-113, DPS-C8-P-113, C8-P-113-8DSS, and

8DSS-C8-P-113 were prepared in 25 % BHI medium. They were then pipetted into a 96-well cell culture plate with the final concentrations from 0.015 to 64 μM mL^{-1} [100 μL $well^{-1}$]. Each well was seeded with 10 μL *S. mutans* suspension, *S. gordonii* suspension, and *S. sanguinis* suspension, respectively. The negative and blank control groups were prepared using 25 % BHI medium with and without bacteria, respectively, in 10 mM HEPES buffer (pH = 7). The bacterial growth was assessed by measuring the absorbance at 595 nm using a microplate reader after a 24-h incubation. Subsequently, 10 μL of bacterial suspension from each well were plated on horse blood agar plates and incubated at 37 °C for 48 h. The antibacterial activities of AMPs were evaluated. The minimal inhibitory concentration (MIC) is defined as the concentration of peptide that results in a minimum of 90 % reduction in absorbance compared to the negative control group [21]. The minimal bactericidal concentration (MBC) is defined as the lowest concentration of peptide that results in no colony formation on agar plates after incubation [22]. AMPs with weaker antibacterial activity (higher MIC) were excluded in the following experiments. A 24h growth curve of *S. mut*ans in the 1/2 × MBC of AMPs with stronger antibacterial activity was investigated.

2.3.2. Anti-S. mutans adhesion ability

Tooth slices ($N = 40$) were autoclave-sterilized, and immersed in 2 × MBC, 4 × MBC, or 8 × MBC of AMPs (in 10 mM HEPES, $n = 4$ for each) with stronger antibacterial activity, or HEPES buffer (control, 10 mM, 100 μL $well^{-1}$, $n = 4$) in duplicate at 37 °C. After overnight incubation, the samples were transferred to a 96-well plate. 200 μL of *S. mut*ans (1×10^6 CFU mL^{-1}) in 25 % BHI + 1 % sucrose (BHIS) was added, followed by incubation at 37 °C for 5 h. The tooth slices were washed once with PBS. One randomly selected tooth slice from each group was stained with the LIVE/DEAD BacLight Bacterial Viability Kit (L7012, Thermo Fisher Scientific, Waltham, USA) and incubated in the dark for 30 min. Confocal Laser Scanning Microscopy (CLSM, Fluoview 1000, Olympus, USA) was used to acquire fluorescence images. The left three tooth slices were used for colony-forming unit (CFU) counting. Three independent biofilm experiments were conducted.

2.3.3. Anti-S. mutans biofilm activity

S. mutans biofilms were cultivated on enamel working surfaces in a 96-well plate. The tooth slices ($N = 52$) were autoclave-sterilized before anti-biofilm activity testing. 200 μL of *S. mutans* in BHIS (1×10^6 CFU mL^{-1}) was added to each well, followed by incubation at 37 °C for 24 h. After incubation, each tooth slice was washed once with PBS. The tooth slices were then incubated in a new 96-well plate containing 2 × MBC, 4 × MBC, 8 × MBC, 16 × MBC AMPs (with stronger antibacterial activity, $n = 4$ for each) + BHIS, or BHIS (control, $n = 4$) in duplicate for 24 h at 37 °C (in 10 mM HEPES). After incubation, tooth slices were washed once with PBS. One randomly selected tooth slice from each group was stained, and fluorescence images were obtained using CLSM. The remaining three tooth slices were used for CFU counting. Three independent biofilm experiments were conducted.

2.4. Characterization of peptides

2.4.1. General properties and Transmission Electron Microscopy

The general properties of peptides, including C8-P-113, DPS-C8-P-113, and 8DSS-C8-P-113, were investigated. The peptides were dissolved in a 10 mM HEPES solution at varied concentrations, with the pH adjusted to 7 using 0.1 M NaOH. The characteristics of the peptides were then observed.

Peptides (C8-P-113, DPS-C8-P-113, and 8DSS-C8-P-113) were characterized by Transmission Electron Microscopy (TEM). A suspension of 1 μM mL^{-1} peptides were ultrasonically diluted with deionized water. The diluted suspension was smeared onto a carbon-coated copper grid (200 mesh). The grids were stained with uranyl acetate solution (2 % w/v in water) for 40 s and washed twice with water. They were then examined under TEM (Philips CM 100, Philips/FEI Corporation, USA).

2.4.2. Field Emission Scanning Electron Microscope

To observe the status of the hydrogel, a concentration of 16 μM mL^{-1} of the peptide 8DSS-C8-P-113 was applied onto a cover slip. The hydrogel 8DSS-C8-P-113 was fixed using 2.5 % glutaraldehyde (Sigma-Aldrich, USA) in PBS (10 mM, pH = 7.2) overnight at 4 °C. Subsequently, the hydrogel was dehydrated using a series of ethanal solutions with increasing concentrations. The dehydrated hydrogel was then subjected to the critical point drying technique. After preparation, the hydrogel sample was cut and the cross-section morphology was analyzed using a Field Emission Scanning Electron Microscope (FE-SEM S4800, Hitachi, Japan).

2.4.3. Stability

Human saliva was collected from a volunteer in the morning prior to oral cleaning with written informed consent, which was approved by the Institutional Review Board of the University of Hong Kong/Hospital Authority Hong Kong West Cluster (IRB No: UW22-657). The collected saliva samples were centrifuged at 12,000 rpm for 20 min [23]. The supernatant was filtered to remove any debris. Peptide solution (C8-P-113, DPS-C8-P-113, or 8DSS-C8-P-113) was added into the human saliva with the final concentration 1 mg mL^{-1}, and then was incubated at 37 °C. At 0, 0.5, 1, 2, 4, and 6 h, 40 μL solutions were taken from each sample and were analyzed by High Performance Liquid Chromatography (HPLC-UV, 1525 Binary HPLC Pump, 2489 UV/Visible Detector, Waters, USA).

20 μL of 16 μM mL^{-1} solution of 8DSS-C8-P-113 was applied to the tooth surface ($N = 5$), and self-formed a layer of hydrogel sticking to the bottom of a hand-made instrument (Fig. 2j). To simulate the average human salivary flow rate, a stable flow of deionized water at a rate of 30 mL h^{-1} was provided using a Syringe Pump (LSP02-1B Double Channel inject/extract, China). The drained liquid, approximately 15 mL, was collected every 30 min. A sample of 100 μL of 16 μM mL^{-1} solution of 8DSS-C8-P-113 was added to 15 mL of deionized water to serve as the 0 min sample. After 2 h, the drained liquids collected at 30 min, 60 min, 90 min, and 120 min were tested for their concentrations using Pierce BCA Protein Assay Kit (Rockford, IL).

2.4.4. Cytocompatibility test

MC3T3-E1 cells (ATCC 2593, ATCC, Manassas, USA) were used to test the toxicity of peptides. MC3T3-E1 cells (5×10^3) were seeded in a 96-well plate and cultured in the alpha minimum essential medium (α-MEM, Thermo Fisher Scientific, USA) at 37 °C under the condition of 95 % air and 5 % CO_2. After 24 h, cells were exposed to peptide solution (C8-P113, DPS-C8-P113, or 8DSS-C8-P113 dissolved in α-MEM) for 24 h at three different concentrations: 1/2 × MBC, MBC, and 2 × MBC in triplicate. Cells exposed to α-MEM without peptide was the control group. Cells viability after peptide exposure was evaluated by cell survival rate using Cell Counting Kit-8 assay (CCK-8 assay, Sigma-Aldrich, USA).

Cells proliferation was tested on peptide-coated enamel surface. Tooth slices ($N = 40$) were immersed in sterilized peptide solution (C8-P113, DPS-C8-P113, 8DSS-C8-P113 at MBC concentration, or 16 μM mL^{-1} of 8DSS-C8-P113, $n = 8$ for each) or deionized water (control, $n = 8$) for 30 min at 37 °C. MC3T3-E1 cells (5×10^3) were seeded onto the peptide-coated enamel working surfaces. After culturing for one and three days, three tooth slices in each group were used to test the proliferation of MC3T3-E1 cells by CCK-8 assay. The tooth slice left in each group was stained by CellTracker Green (C7025, Thermo Fisher Scientific, USA). Fluorescence images were taken with CLSM.

2.5. Remineralization assay of peptides

The enamel surfaces of tooth slices ($N = 30$) were subjected to acid-etching in 37 % phosphoric acid for 1 min, followed by rinsing with

deionized water for 1 min. Solutions of C8-P113, DPS-C8-P113, 8DSS-C8-P113 (at MBC concentration, in 10 mM HEPES), or HEPES (control) were then added in 5 μL droplets onto the tooth slices ($n = 5$ for each). To investigate the impact of hydrogel status on remineralization, 16 μM mL^{-1} 8DSS-C8-P113 ($n = 5$) was also added in 5 μL droplets onto the tooth slices. The hydrogel control group ($n = 5$) consisted of dissolving 0.5 g of agarose powder in 100 mL of deionized water, adjusting the pH to 6.5 using 0.1 M NaOH, heating to 100 °C, and keeping at 60 °C after complete dissolution before use [24]. Following natural drying of the liquids or formation of hydrogels, all tooth slices were incubated in 6 mL of remineralization solution (2.58 mM $CaCl_2{\cdot}2H_2O$, 1.55 mM KH_2PO_4, 1 mg L^{-1} NaF, 180 mM NaCl, 50 mM Tris-HCl, pH = 7.6) for 1 day, 3 days, and 7 days, respectively [25]. The remineralization solutions were replaced daily. The enamel surface and cross-section morphology were analyzed using a FE-SEM. The Vicker's hardness of the enamel on the tooth slices was measured using a Microhardness tester (MCT^3, Anton Paar, Australia). The enamel surface was subjected to a load of 0.5 N for 10 s at each test point for microhardness assessment.

2.6. Demineralization assay in the artificial caries model

Tooth slices ($N = 30$) were autoclave-sterilized and then were immersed in C8-P113, DPS-C8-P113, 8DSS-C8-P113 solutions (at MBC concentration, in 10 mM HEPES) or HEPES (control) ($n = 5$ for each) overnight. To investigate the impact of hydrogel status on demineralization, 16 μM mL^{-1} 8DSS-C8-P113 ($n = 5$) was also added in 5 μL droplets onto the tooth slices. The control group ($n = 5$) consisted of dissolving 0.5 g of agarose powder in 100 mL of deionized water, adjusting the pH to 6.5 using 0.1 M NaOH, heating to 100 °C, and keeping at 60 °C after complete dissolution before use [24]. After natural drying of the liquids or formation of hydrogels, all tooth slices were put into 24-well plate. A 700 μL suspension of *S. mutans* (1×10^6 CFU mL^{-1}) in BHIS was added to a 24-well plate and incubated at 37 °C for 7 days. On the 1st day, 3rd day, 5th day, and 7th day, tooth slices were transferred to new wells adding BHIS. After 7 days, tooth slices were scanned by MicroCT and the lesion depth and mineral density of lesions were evaluated by CT Analyzer software (ver. 1.20.3.0+, Bruker MicroCT, USA). The random five areas on each tooth slice were measured.

2.7. The mechanism of antibacterial activity of the optimal multi-functional peptide

2.7.1. Lactate dehydrogenase assay

A series of two-fold dilutions of 8DSS-C8-P-113 peptide at sub-MBC levels (1/2 × MBC, 1/4 × MBC, and 1/8 × MBC, $n = 5$ for each) were prepared in BHIS medium. *S. mutans* cells were individually exposed to the 8DSS-C8-P113 peptide solutions and cultivated for a duration of 24 h. The control group consisted of *S. mutans* cells cultivated in BHIS media without 8DSS-C8-P-113 ($n = 5$). To assess the activity of lactate dehydrogenase (LDH) assay, the LDH Activity Assay Kit (MAK066, Sigma-Aldrich, USA) was used. After incubation, the samples were homogenized on ice in LDH assay buffer. The resulting homogenate was then centrifuged (3000 rpm, 15 min, 4 °C). The supernatant containing the released LDH enzyme was collected for further analysis. To quantify the LDH enzymatic activity, the absorbance at 450 nm was measured, following the instructions provided with the LDH Activity Assay Kit. The recorded absorbance values were used to calculate the percentage of ΔA450 (change in absorbance at 450 nm) relative to the untreated control. Three independent LDH assays were conducted.

2.7.2. Water-insoluble extracellular polysaccharides measurement

Biofilms of *S. mut*ans were generated in 96-well plates using different sub-MBC levels (1/2 × MBC, 1/4 × MBC, and 1/8 × MBC, $n = 5$ for each) of 8DSS-C8-P113 peptide in BHIS medium. BHIS medium was the control group ($n = 5$). To determine the water-insoluble extracellular polysaccharides (EPS) in the biofilms, the anthrone method was employed [26]. To collect the biofilms, they were subjected to sonication in PBS buffer. The resulting precipitate was obtained through centrifugation (6000 rpm, 10 min) and then resuspended in 200 μL of 0.4 M NaOH. The suspension was incubated at 37 °C for 2 h. Following another round of centrifugation (6000 rpm,10 min), 100 μL of the supernatant was mixed with 300 μL of anthrone reagent and heated at 95 °C for 8 min. The absorbance at 625 nm was measured to quantify the EPS content. This process was repeated three times independently.

For EPS staining, biofilms of *S. mutans* were developed on tooth slices ($N = 20$) in a 96-well plate using different sub-MBC levels (1/2 × MBC, 1/4 × MBC, and 1/8 × MBC, $n = 5$ for each) of 8DSS-C8-P113 in BHIS medium. BHIS medium was the control group ($n = 5$). At the start of biofilm formation, Alexa Fluor® 647 (D22914; Molecular Probes™) was added, while SYTO®9 (S34854; Molecular Probes™, Invitrogen, Carlsbad, CA) was used to stain the bacteria after biofilm formation. CLSM was utilized to image the biofilms. Each biofilm was scanned at five randomly selected positions. The three-dimensional (3D) reconstructions of the biofilms were performed using ZEN 3.3 software (Carl Zeiss, Germany). The calculation of bacteria/EPS biomass was conducted using COMSTAT [27].

2.7.3. Transcriptome analysis

S. mutans were treated with 1 μM mL^{-1} (1/2 × MBC) 8DSS-C8-P113 in BHI medium (pH = 7) for 24 h at 37 °C, and BHI medium without 8DSS-C8-P113 was used as the control group. The cells in two groups were collected after centrifugation at 10000 rpm under 4 °C for 2 min. Total bacterial RNA was extracted by utilizing the Trizol Reagent (Invitrogen, Carlsbad, CA, USA). The quality and integrity of extracted RNA were determined by NanoDrop 2000 spectrophotometer (Thermo Scientific, Wilmington, USA) and Bioanalyzer 2100 system (Agilent Technologies, Santa Clara, CA, USA), respectively. After removing rRNA and constructing cDNA libraries, the libraries were sequenced based on NovaSeq 6000 platform (Illumina, San Diego, USA) by Shanghai Personal Biotechnology Cp. Ltd (Shanghai, China).

After quality assessment and filtering of raw data, the libraries were used for subsequent bioinformatics analysis. According to reference genome (NCBI genome sequencing GCF_009738105.1), the filtered data were annotated utilizing Bowtie 2 software (version 2.2.6.). The value of fragments per kilobase per million mapped reads (FPKM) was used to represent the expression level of each gene. Then, DESeq R package (version 1.30.0) was then used to perform differential expression analysis to identify differentially expressed genes (DEGs). The mRNAs with $|\log_2\text{fold change}| > 1$ and $p < 0.05$ were considered as DEGs between control and experimental groups. The volcano plot and heatmap of DEGs were generated using ggplot2 R package. Gene Ontology (GO) enrichment analysis was conducted by ClusterProfiler (version 3.4.4) and topGO to determine underlying biological function, while Kyoto Encyclopedia of Genes and Genomes (KEGG) pathway enrichment analysis was carried out by ClusterProfiler (version 3.4.4) to investigate the potential mechanisms involved in the antimicrobial effects of 8DSS-C8-P113. The GO terms and KEGG pathways with *P* 0.05 were considered significantly enriched by DEGs. The ggplot2 package was applied to generate bar charts of GO terms and KEGG pathways.

2.8. Molecular dynamic analysis

2.8.1. The formation of 8DSS-C8-P113 hydrogel

Based on the experiment of 8DSS-C8-P113 self-forming a hydrogel structure in deionized water, MD analysis was used to stimulate the process and create a 3D model. AlphaFold software was used to create one 8DSS-C8-P113 molecule structure. A simulated box measuring 10 nm × 10 nm × 10 nm was constructed and 20 of 8DSS-C8-P113 molecules were added into the box. MD simulation was carried out using Gromacs 2019.6 program under constant temperature and pressure with

Table 2
MBCs of peptides against bacteria.

Strains	MBC (μM mL^{-1})								
	P-113	P-113-DPS	DPS-P-113	P-113-8DSS	8DSS-P-113	C8-P-113	DPS-C8-P-113	C8-P-113-8DSS	8DSS-C8-P-113
S. mutans	>128.00	16.00	64.00	>64.00	>64.00	0.03	0.25	64.00	2.00
S. gordonii	>128.00	>64.00	>64.00	>64.00	64.00	0.25	4.00	>64.00	32.00
S. sanguinis	>128.00	>64.00	>64.00	>64.00	64.00	0.25	2.00	>64.00	32.00

periodic boundary conditions [28]. The cluster module of Gromacs was used to analyze the simulation trajectories from 60 to 100 ns, with a root mean square deviation (RMSD) cut-off value of 1.2 nm. The final configuration was established. To further investigate the intermolecular interactions in peptide aggregation, the plugin gmx_energy was utilized to compare and analyze the interaction energies (including hydrogen bonding, hydrophobic interactions, and electrostatic interactions) and the quantities of various interactions among peptide molecules in the entire system.

2.8.2. Remineralization system

MD simulation was employed to investigate the interaction between hydrogel structures of 8DSS-C8-P113 and HAP crystal surfaces, as well as the interactions between HAP crystal surfaces and ions (Ca^{2+}, HPO_4^{2-}, $H_2PO_4^-$). Due to the lower hydration energy of calcium ions on the surface of HAP, HAP (100) and HAP (001) surfaces with high calcium ion content were constructed separately. The crystal model of HAP (100) has dimensions of 11.31 nm × 13.07 nm × 22.00 nm in the xyz direction, while the crystal model of HAP (001) has dimensions of 11.31 nm × 13.06 nm × 22.00 nm in the xyz direction. Twenty 8DSS-C8-P113 hydrogel structures, Ca^{2+}, HPO_4^{2-}, and $H_2PO_4^-$, were added to each of the two systems HAP (100) surface and HAP (001) surface. MD simulation was conducted using the Gromacs 2019.6 program with constant temperature and pressure and periodic boundary conditions [28]. The two systems were simulated for 100 ns, with conformations saved every 20 ps. The interactions between peptide clusters and HAP surfaces, spatial conformations, and the distance between the centroids of the two systems were analyzed at the end of each simulation. The radial distribution function of free Ca^{2+} ions and phosphorus atoms on the HAP surface, as well as the interaction energy between free phosphate ions (HPO_4^{2-}, $H_2PO_4^-$) and Ca^{2+} ions on the HAP surface were also analyzed. The simulation results were visualized using the built-in program in Gromacs and Visual Molecular Dynamics (VMD).

2.9. Rat caries model

The rat caries model was conducted under the protocol approved by the Ethics Committee of Anhui Medical University, China (ref. no. LLSC20232002) in accordance with national and international guidelines to minimize animal suffering. Ten male specific pathogen-free Sprague-Dawley rats aged 6 weeks were selected. The rats were provided with appropriate antibiotics (ampicillin, chloramphenicol, and carbencillin 1.0 g/kg/day) in the drinking water for 3 days. Then the rats were orally infected with 0.3 mL fresh BHI medium containing *S. mutans* (10^9 CFU mL^{-1}) once a day for 10 days. The infection was confirmed by oral swabbing and culturing on mitis salivarius-bacitracin (MSB) agar plates. The infected animals were randomly assigned into two groups ($N = 10$): 16 μM mL^{-1} of 8DSS-C8-P-113 in 10 mM HEPES (pH = 7, $n = 5$) and 10 mM HEPES ($n = 5$, control group). Animals in each group were treated with 150 μL of the respective treatment topically using dental bonding brush for 2 min once daily for 4 weeks. The rats were fed with cariogenic Keyes 2000 diet (Jiangsu Xietong Pharmaceutical Bio-engineering Co., Ltd, Nanjing, China) and 5 % sucrose water ad libitum during the inoculation of *S. mutans* and the 4-week treatment [29]. After the rats were sacrificed, the lower jaw was aseptically dissected and sonicated in 5.0 mL of sterile saline solution (0.9 %, w/v). The obtained suspensions were streaked on MSB agar plates to estimate the population of *S. mutans*. The lower left molars of the rats were scanned using MicroCT to analyze the volume of dental caries. The 3D reconstructions of the tooth crown and tooth half-crown were conducted by the CTVOL software (ver. 2.3.2.0, Bruker MicroCT, USA). All molars were cut from mesial to distal, the cross sections were photographed using the stereo microscope (Nikon SM218, USA). The severity of caries was evaluated by the Keyes' scoring system which categorizes caries as enamel only (E), dentin exposed 1/4 to 3/4 (Ds), or more than 3/4 dentin affected (Dm) [30,31]. The rats' weights were recorded to monitor for signs of toxicity. Additionally, various tissues from gingiva, palate, heart, liver, spleen, lung, and kidney were collected, stained with hematoxylin and eosin (H&E), and histopathologically analyzed [32].

2.10. Statistics

Statistical analyses were performed using SPSS 27.0 software (IBM Corporation, Armonk, NY, USA). ANOVA was utilized to assess means with more than two groups, and Tukey HSD tests were employed to determine their mutual significance. Data are presented as mean ± standard deviation, and $p < 0.05$ is regarded as statistically significant ($^*p < 0.05$, $^{**}p < 0.01$, $^{***}p < 0.001$).

3. Results and discussion

3.1. Anti-bacterial ability

3.1.1. Anti-planktonic S. mutans, S. Gordonii and S. Sanguinis

The susceptibility assay for planktonic *S. mutans*, *S. gordonii* and *S. sanguinis* in peptides is summarized in Table 2. MICs could not be tested due to precipitation of peptides. C8-P-113, DPS-C8-P-113, and 8DSS-C8-P-113 showed stronger anti-planktonic *S. mutans* activity than other peptides, based on their lower MBC values (0.03 μM mL^{-1}, 0.25 μM mL^{-1}, and 2.00 μM mL^{-1}, respectively). Furthermore, C8-P-113 showed 8-fold difference in susceptibility between against *S. mutans* (0.03 μM mL^{-1}) and other two bacteria, *S. gordonii* and *S. sanguinis* (0.25 μM mL^{-1}). Susceptibility against *S. mutans* was also found in DPS-C8-P-113 (0.25 μM mL^{-1}) and 8DSS-C8-P-113 (2.00 μM mL^{-1}). Only C8-P-113, DPS-C8-P-113 and 8DSS-C8-P-113, presented enhanced antimicrobial activity and specificity against planktonic *S. mutans* cells; therefore, other peptides were excluded from the following experiments. P-113 and the modified P-113 peptides presented the broad-spectrum antibacterial activities to *S. mutans*, *S. gordonii* and *S. sanguinis*. Peptides with the competence stimulating peptide fragment C8 presented specific targeting ability in this study, killing *S. mutans* with lower concentrations and protecting the oral normal flora, such as *S. gordonii* and *S. sanguinis*. These results are consistent with findings from a previous study [13]. Based on results from C8-P-113, DPS-C8-P-113, and 8DSS-C8-P-113, it is noted that P-113 in the C-terminus exhibits better antibacterial activities to *S. mutans*. C8-P-113-8DSS needs a higher concentration against *S. mutans*, *S. gordonii* and *S. sanguinis*. The competence stimulating peptide in the N-terminus and non-specific AMP in the C-terminus have better efficacy, which coincides with other studies [13,33]. Syvitski et al. have worked on the signalling molecule of the quorum sensing (QS) circuit in *S. mutans* and found that the C terminus might be important for activation of the signalling pathway [34].

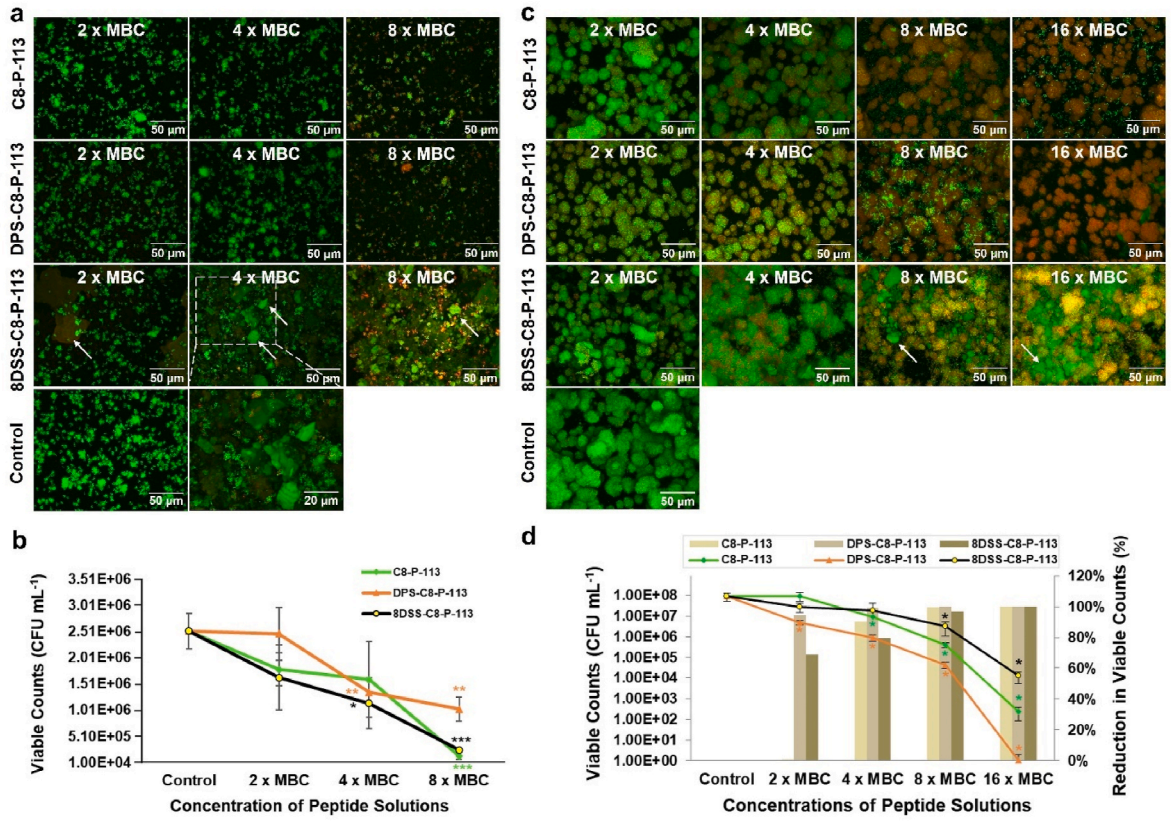

Fig. 1. Anti-*S. mutans* adhesion and anti-*S. mutans* biofilm activity of peptide solution. (a) Fluorescence images (× 60) of *S. mutans* adhesion on peptide-coated enamel surfaces in different groups with varied concentrations. (b) Viable counts of *S. mutans* adhesion on peptide-coated enamel surfaces after 5 h of incubation. (c) Fluorescence images (× 60) of *S. mutans* biofilms in peptide solutions with different concentrations. (d) Viable counts (left: ordinate and point plot) and percentage reduction in viable counts (right: ordinate and bar chart) of *S. mutans* biofilms after 24 h of exposure to peptide solutions with varied concentrations. *$p <$ 0.05, **$p < 0.01$, ***$p < 0.001$, compared with control group. 8DSS-C8-P-113 hydrogel peptide was stained green and indicated by arrows.

3.1.2. Growth inhibition

S. mutans in the 1/2 × MBC of C8-P-113, DPS-C8-P-113, or 8DSS-C8-P-113 solutions continued to grow approximately at the same rate within the first 5 h, compared with the control group (Fig. S3). The absorbance of 8DSS-C8-P-113 suspension was higher even in the very beginning due to its innate translucency. *S. mutans* started to grow exponentially from 5 h and reached a growth plateau around 12 h in all groups. A decrease in *S. mutans* growth was observed after a longer exposure to 1/2 × MBC peptides. C8-P-113, DPS-C8-P-113, and 8DSS-C8-P-113 exhibited inhibitory effect on the *S. mutans* growth.

3.1.3. Anti-S. mutans adhesion ability

After 5 h of exposure of *S. mutans* to the peptide-coated enamel surfaces, the CLSM images of 8 × MBC C8-P-113-coated, DPS-C8-P-113-coated, or 8DSS-C8-P-113-coated enamel surfaces revealed less live *S. mutans* (green) than the non-coated enamel surfaces in the control group (Fig. 1a). The fragments of 8DSS-C8-P-113 hydrogel that formed crystal-like structures on the surface of enamel surface were stained green (indicated by arrows) and have a completely different morphology from *S. mutans* colonies. Some dead *S. mutans* (red) can be found on the enamel surface in the 8 × MBC DPS-C8-P-113 group and 8 × MBC 8DSS-C8-P-113 group (Fig. 1a). The viable counts of *S. mutans* were significantly reduced with 8 × MBC C8-P-113-coated [1.31E + 05 (CFU mL^{-1}), $p < 0.001$], 8 × MBC DPS-C8-P-113-coated [1.02E + 06 (CFU mL^{-1}), $p < 0.01$], 8 × MBC 8DSS-C8-P-113-coated [2.49E + 05 (CFU mL^{-1}), $p < 0.001$] enamel surfaces compared with non-coated enamel surfaces [2.52E + 06 (CFU mL^{-1})] (Fig. 1b). At the concentration of 4 × MBC, viable counts of *S. mutans* on the C8-P-113-coated enamel surface showed no significantly different with that in the control group. In comparison with C8-P-113, DPS-C8-P-113 and 8DSS-C8-P-113 showed more potent inhibitory effects on the *S. mutans* adhesion.

3.1.4. Anti-S. mutans biofilm ability

After 24 h of exposure of *S. mutans* biofilms to C8-P-113 and DPS-C8-P-113 solutions, the majority of *S. mutans* were dead (red, Fig. 1c) as shown in CLSM images with concentrations of 8 × MBC and 16 × MBC. In contrast, the majority of *S. mutans* in the control group were alive (green, Fig. 1c). In the 8 × MBC and 16 × MBC concentrations of the 8DSS-C8-P-113 group, numerous biofilms appeared yellow (indicated by arrows) due to the mixture of green staining of 8DSS-C8-P-113 hydrogel and red staining of dead *S. mutans*, (Fig. 1c). Approximately 99.00 %, 99.35 %, and 100 % *S. mutans* were killed at the concentration 4 × MBC, 8 × MBC, and 16 × MBC of DPS-C8-P-113, respectively (Fig. 1d). The viability by CFU counts in the 4 × MBC DPS-C8-P-113 group [9.16E + 05 (CFU mL^{-1})], 8 × MBC DPS-C8-P-113 group [4.38E + 05 (CFU mL^{-1})], and 16 × MBC DPS-C8-P-113 group [0 (CFU mL^{-1})] were significantly lower than the control group [9.20E + 07 (CFU mL^{-1})] ($p < 0.05$, Fig. 1d). Approximately 96.59 % and 99.98 % *S. mutans* were killed by 8 × MBC and 16 × MBC of 8DSS-C8-P-113, respectively. The viability by CFU counts in the 8 × MBC 8DSS-C8-P-113 group [3.14E + 06 (CFU mL^{-1})] and 16 × MBC 8DSS-C8-P-113 group [1.25E + 05 (CFU mL^{-1})] were significantly lower than the control group [9.20E + 07 (CFU mL^{-1})] ($p < 0.05$, Fig. 1d). Approximately 90.39 %, 99.55 %, and 100 % *S. mutans* were killed at the concentration 4 × MBC, 8 × MBC, and 16 × MBC of C8-P-113, respectively (Fig. 1d). Even though the residual *S. mutans* atop deceased bacteria may potentially compromise the antibacterial effectiveness, it is crucial to acknowledge the hydrogel characteristics of 8DSS-C8-P-113, which

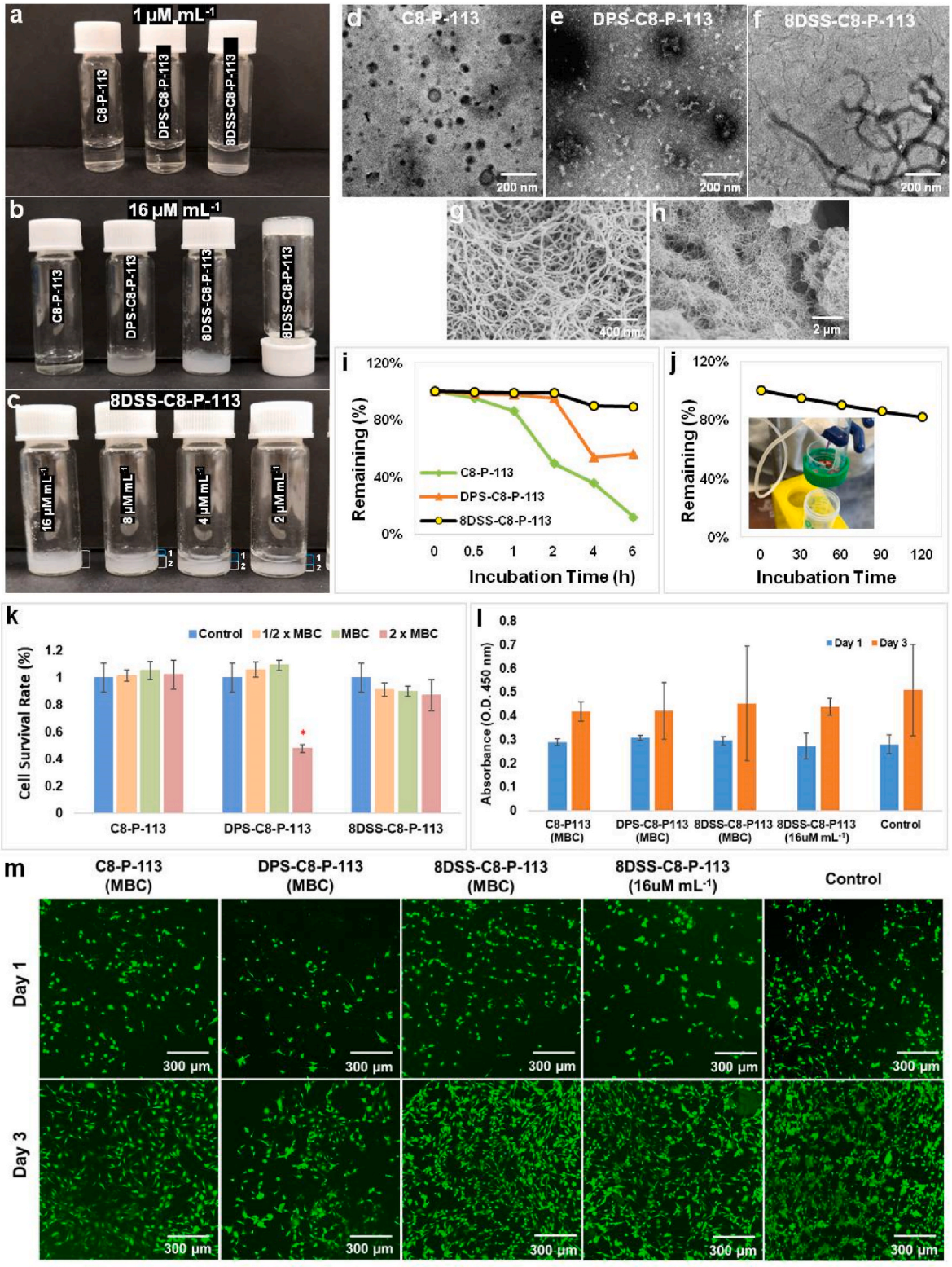

Fig. 2. Characterization, TEM micrographs, stability, and cytocompatibility of peptides. (a) 1 μM mL^{-1} C8-P-113, DPS-C8-P-113 and 8DSS-C8-P-113 in HEPES (pH = 7). (b) 16 μM mL^{-1} C8-P-113, DPS-C8-P-113 and 8DSS-C8-P-113 in HEPES (pH = 7) after 10 min dissolving. (c) 8DSS-C8-P-113 at concentrations of 16, 8, 4, and 2 μM mL^{-1}, with a distinct two-layer status observed at the latter three concentrations. (d–f) TEM micrographs (× 10,000) of C8-P-113, DPS-C8-P-113 and 8DSS-C8-P-113. (g–h) FE-SEM micrographs of 8DSS-C8-P-113 hydrogel (× 50,000) and 8DSS-C8-P-113 hydrogel (× 10,000). (i) Changes in remaining percentage of peptides incubated in human saliva at 37 °C during 6 h. (j) Changes in remaining percentage of 8DSS-C8-P-113 hydrogel incubated in flow water at the rate of 30 mL h^{-1} during 2 h. (k) Cell survival rate after cells exposed at peptide solution for 24h. *$p < 0.05$, compared with control. (l) Proliferation of MC3T3-E1 on peptide-coated enamel surfaces for 1 and 3 days. (m) Fluorescence images of MC3T3-E1 on peptide-coated enamel surfaces for 1 and 3 days (× 10).

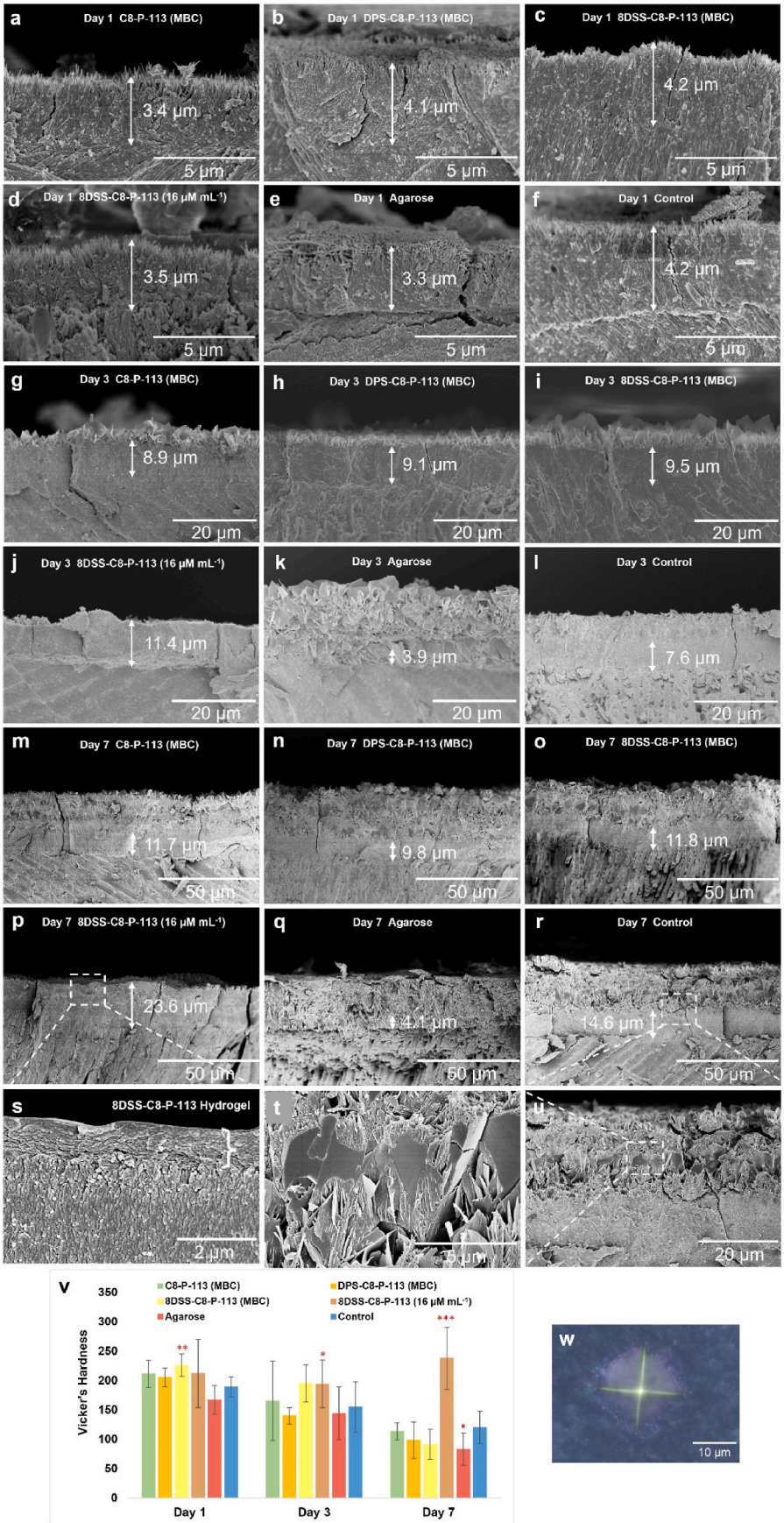

(caption on next page)

Fig. 3. Remineralization assay. The arrows indicate the thickness of needle-like crystals. (a–f) FE-SEM micrographs (× 10,000) of the remineralization cross-sections in C8-P-113 (MBC), DPS-C8-P-113 (MBC), 8DSS-C8-P-113 (MBC), 8DSS-C8-P-113 (16 μM mL^{-1}), agarose, and control group on the 1st day. (g–l) FE-SEM micrographs (× 2000) in different groups on the 3rd day. (m–r) FE-SEM micrographs (× 1000) in different groups on the 7th day. (s) Magnification of micrograph (p) (× 20,000). The big brace indicates the thickness of the 8DSS-C8-P-113 hydrogel layer. (t) Magnification of micrograph (u) (× 10,000). (u) Magnification of micrograph (r) (× 2000). (v) Vicker's hardness of different surface treated-enamel specimens after 1 day, 3 days, and 7 days of incubation in the remineralization solution. *$p < 0.05$, **$p < 0.01$, ***$p < 0.001$, compared with control group on the same day. (w) The indentation made on the remineralized tooth surface.

could facilitate sustained release, potentially affecting the activity of surviving *S. mutans*. All of them at the 8 × MBC and 16 × MBC presented significant killing to the *S. mutans* biofilm. In contrast, DPS-C8-P-113 exhibited the most potent inhibitory effects on the eradication of *S. mutans* biofilm. The addition of improving remineralization sequences with DPS and 8DSS may increase the peptides' adsorption on the enamel surface to prevent *S. mutans* adhesion [18,35]. Another potential explanation for the reduction in *S. mutans* adhesion and the eradication of *S. mutans* biofilm could be attributed to the involvement of DPS-C8-P-113 or 8DSS-C8-P-113 in modulating the metabolism or QS of *S. mutans*, leading to a decrease in its virulence and colony formation. This hypothesis will be elaborated in Section 3.5.

3.2. Characterization of peptides

3.2.1. Physical properties of peptides

The characterization of C8-P-113, DPS-C8-P-113, and 8DSS-C8-P-113 was evaluated, with their respective isoelectric points (pI) being 12.15, 12.15, and 6.35. In HEPES (concentration: 1 μM mL^{-1}, pH = 7), C8-P-113 and DPS-C8-P-113 were colorless transparent liquids, while 8DSS-C8-P-113 presented a white suspension as depicted in Fig. 2a. After 10 min of dissolving in HEPES (pH = 7), 16 μM mL^{-1} C8-P-113 remained a colorless transparent liquid, while DPS-C8-P-113 formed a white suspension at the same concentration. In contrast, 16 μM mL^{-1} 8DSS-C8-P-113 formed a hydrogel, as illustrated in Fig. 2b. The thick hydrogel adhered to the bottom of an inverted vial. Furthermore, the 2-fold diluted series of 8DSS-C8-P-113 displayed a two-layer status at concentrations of 8, 4, and 2 μM mL^{-1}, respectively, without achieving hydrogel formation. (Fig. 2c).

3.2.2. TEM micrographs of peptides

TEM micrographs revealed distinct morphologies for each peptide. C8-P-113 exhibited a spherical particle shape with a diameter of 100 nm (Fig. 2d), while DPS-C8-P-113 had a short linear shape with a length of 100–150 nm and a width of 25–33 nm (Fig. 2e). In contrast, 8DSS-C8-P-113 displayed a 3D fiber network with helical twists, as illustrated in Fig. 2f. The fibers were approximately 30 nm wide and varied in length, often appearing very long.

3.2.3. FE-SEM micrographs of 8DSS-C8-P-113 hydrogel

After fixation and dehydration, a 3D fiber network of 8DSS-C8-P-113 hydrogel was observed by FE-SEM (Fig. 2g and h). The fibers in the network were approximately 30 nm in width, and the hydrogel exhibited pore sizes with a diameter of around 500 nm.

3.2.4. Stability of peptides

The changes in the remaining percentage and concentration of peptides incubated in human saliva are shown in Fig. 2i and Table S1, respectively. C8-P-113 remained 11.9 %, DPS-C8-P-113 remained 56.2 %, and 8DSS-C8-P-113 remained 89.4 % intact after being incubated in human saliva at 37 °C for 6 h. Fig. 2j illustrates the changes in the remaining percentage of 8DSS-C8-P-113 hydrogel when incubated in flow water at a rate of the 30 mL h^{-1}. After 2 h, 8DSS-C8-P-113 hydrogel maintained approximately 82.15 % of its initial status on the tooth surface. The hydrogel's dissolving percentage was approximately 4.46 % every 30 min. These results demonstrate that 8DSS-C8-P-113 exhibits desirable stability in human saliva. According to the results of TEM and FE-SEM, the 3D fiber network with helical twists may contribute to its stability in the aqueous environment. The stability is further strengthened by the 3D fiber network when 8DSS-C8-P-113 transitions into a hydrogel on the tooth surface. The adhesion of the hydrogel to the tooth surface enhances its stability compared to the peptide in other forms.

3.2.5. Cytocompatibility of peptides

After a 24-h incubation, there were no significant differences in cell survival rates in all concentrations of C8-P-113, 1/2 × MBC and MBC DPS-C8-P-113, and all concentrations of 8DSS-C8-P-113, when compared to the control group (Fig. 2j). The survival rate of DPS-C8-P-113 at 2 × MBC concentration decreased to 48 %. Additionally, after 1 and 3 days of incubation, the proliferation of MC3T3-E1 cells on peptide-coated enamel surfaces was not significantly different among all groups (Fig. 2k). Results from fluorescent images (Fig. 2l) were consistent with the quantitative CCK-8 assay. MC3T3-E1 cells were stained green and exhibited a spindle-like morphology in all groups after 3 days of incubation. During the 3-day incubation period, peptide-coated groups showed a significantly increasing number of live cells, which was similar to that observed in the control group. These results indicate that C8-P-113, DPS-C8-P-113, and 8DSS-C8-P-113 have good cytocompatibility at MBC concentration. Furthermore, the hydrogel formed from 16 μM mL^{-1} of 8DSS-C8-P-113 was also found to be safe.

Based on the arrangement and combination of the three functional parts, i.e., P-113 (the AMP), C8 (the competence stimulating peptide), and DPS/8DSS (the domains of improving remineralization), 12 new molecules can be fabricated. However, considering the function of specific antimicrobial activities, the sequence of C8-P-113 is a better design. DPS/8DSS was planned to be in the end of C-terminus or N-terminus to design four molecules, including C8-P-113-DPS, DPS-C8-P-113, C8-P-113-8DSS, 8DSS-C8-P-113. Nevertheless, C8-P-113-DPS could not be synthesized due to the weak stability during fabrication (Table 1). C8-P-113-8DSS has weaker antibacterial activity against *S. mutans* (Table 2). DPS-C8-P-113 and 8DSS-C8-P-113 have good stability and cytocompatibility, which demonstrates that the domain of improving remineralization in the N-terminus is better than that in the C-terminus. Since 8DSS-C8-P-113 with a concentration of 16 μM mL^{-1} can self-form hydrogels, the 3D network structure of this status absorbs a large amount of water [36,37]. Hydrogels are hydrophilic polymers that have properties of flexibility, porosity, soft structure, biodegradability, biocompatibility, low immunogenicity, and ease of usage [38,39]. Because of these advantages, they have been applied in many fields, such as drug delivery, tissue engineering and regenerative medicine [40]. In this study, the 16 μM mL^{-1} 8DSS-C8-P-113 remained over 80 % hydrogel status on the tooth surface even after exposing to a simulated salivary flow environment for 2 h. This safe and stable hydrogel may potentially offer protection to the tooth against damage from bacteria and acid.

3.3. Remineralization property

After exposure of enamel surfaces to remineralization solutions for one day, new HA crystals as imaged by FE-SEM were formed on demineralized enamel slices in all groups (Fig. 3a–f). Cross-sectional micrographs of the remineralized enamel slices clearly showed a newly regenerated layer tightly conjoined to its underlying natural enamel. The thickness of the regenerated crystal layer on the enamel surface among different groups showed no significant difference (around 4 μm), see Fig. 3a–f. The crystal macrostructure of the regenerated layer was

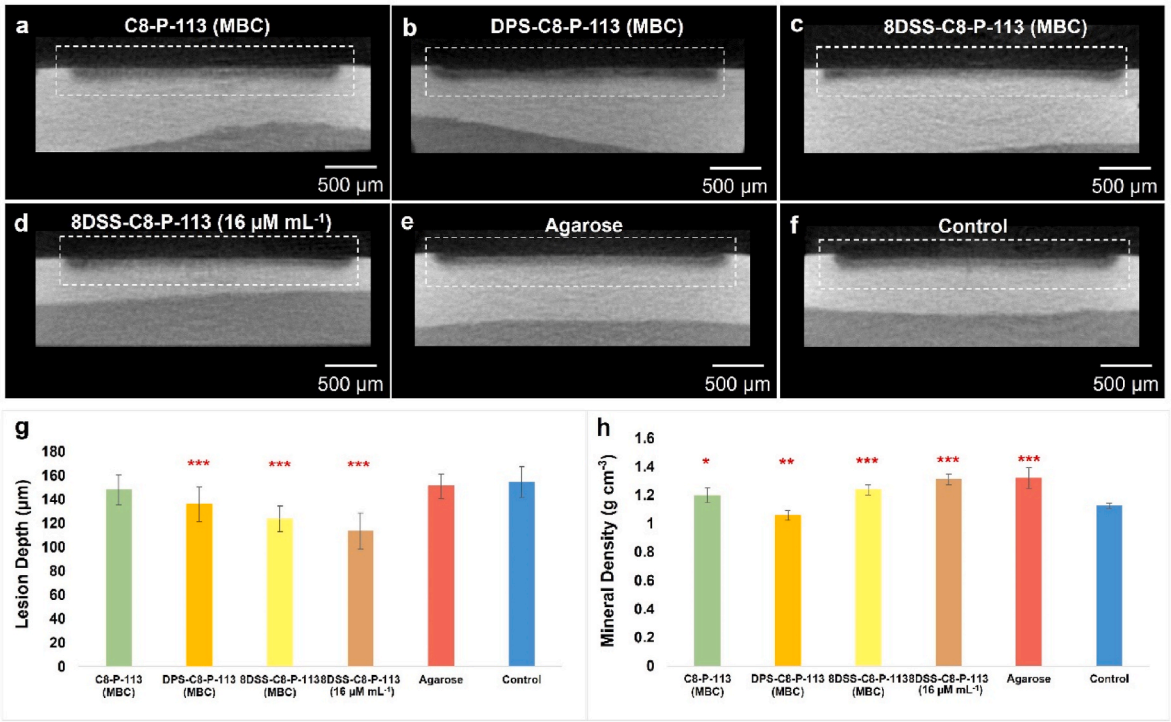

Fig. 4. The cross-section of lesions on the enamel surface in the artificial caries models. (a–f) MicroCT graphs (× 50) of the demineralization cross-sections in C8-P-113 (MBC), DPS-C8-P-113 (MBC), 8DSS-C8-P-113 (MBC), 8DSS-C8-P-113 (16 μM mL^{-1}), agarose, and control group. (g) Lesion depth on enamel surfaces. (h) Mineral density of lesion on enamel surfaces. *$p < 0.05$, **$p < 0.01$, ***$p < 0.001$, compared with control group.

needle-like. However, a layer of thick plate-like crystals formed on the needle-like crystals on the 3rd day in all groups except for the 8DSS-C8-P-113 (16 μM mL^{-1}) group (Fig. 3g-l). The layer of plate-like crystals became thicker on the 7th day in all groups except for the 8DSS-C8-P-113 (16 μM mL^{-1}) group (Fig. 3m-r). In the 8DSS-C8-P-113 (16 μM mL^{-1}) group, the regenerated crystal macrostructure consistently exhibited needle-like crystals. On the 3rd day, the crystals had a thickness of 11.4 μm, which increased to 23.6 μm by the 7th day. The mean values of Vicker's hardness of 8DSS-C8-P-113 (MBC) group on the 1st day was 226.94 ± 19.61 HV, which was significantly higher than that of control group on the 1st day (189.77 ± 17.44 HV, **$p < 0.01$) (Fig. 3v). The mean values of Vicker's hardness of 8DSS-C8-P-113 (16 μM mL^{-1}) group on the 3rd day was 194.78 ± 24.96 HV, which was significantly higher than that of control group on the 3rd day (155.45 ± 43.91 HV, *$p < 0.05$) (Fig. 3v). 8DSS-C8-P-113 (16 μM mL^{-1}) group on the 7th day had the highest mean value of Vicker's hardness (238.89 ± 53.24 HV), whereas agarose group has the lowest (83.01 ± 28.74 HV), compared with control group (120.24 ± 28.14 HV) on the 7th day (***$p < 0.001$, *$p < 0.05$) (Fig. 3v). The Vickers hardness decreased over time in all groups except the 8DSS-C8-P-113 (16 μM mL^{-1}) group. A probable explanation is that the development of plate-like crystals on the surface are sparse and exhibit weaker strength.

There are variations in the concentration of fluoride used in different remineralization solution recipes. Some recipes include large doses of fluoride, such as 1100 ppm NaF, 225 ppm NaF, or 10 ppm NaF [18,41,42]. Since chronic fluoride toxicity is associated with excessive fluoride intake, the 'optimal' concentration of fluoride in drinking water is recommended to be 1 ppm [43]. At this level, there is a decrease in caries incidence while maintaining a minimal risk of dental fluorosis. Fan et al. discovered that 1 ppm fluoride was effective to manipulate forming needle-like (hexagonal prisms structure) instead of porous plate-like HAP nanocrystals [44]. In order to reduce the side effects of fluoride, 1 ppm fluoride was used in this study. When incubating for one day, the regenerated minerals tended to be needle-like crystals, which is consistent with the findings of Fan et al. However, as the process time prolonged to 7 days, the regenerated minerals tended to be plate-like crystals. This finding coincides with the study conducted by Andrea Ruffini et al. [45]. Prolonged heating time could influence the aggregation and morphology of HAP through a rearrangement of the built nanostructures, which may alter needle-like to plate-like crystals [45]. Apart from process time, other parameters like Ca/P molar ratio concentration, temperature, pH, or additives also contribute to the final structure of HAP, including needles, plates, and spherical-shaped, with various sizes [46,47]. Based on the results of this study, 16 μM mL^{-1} 8DSS-C8-P-113 group still presented excellent needle-like crystals after incubation for 7 days, with the highest microhardness value. In order to investigate the physical effects of hydrogel status of 8DSS-C8-P-113 on remineralization, agarose with hydrogel status was used to be the control in this study. However, agarose hydrogel on tooth surface could not improve the microhardness of regenerated layers due to the formation of a lot amount of plate-like crystals. Hydrogels formed from 16 μM mL^{-1} 8DSS-C8-P-113 may react with calcium ions, phosphate ions, or fluoride ions; therefore, they could be used as an additive to manipulate crystal structure on the tooth surface during remineralization.

On Day 1, the thickness of remineralized needle-like crystals appeared similar in both the 8DSS-C8-P-113 (MBC) group (Fig. 3c) and the 8DSS-C8-P-113 (16 μM mL^{-1}) group (Fig. 3d). By Day 3, the thickness of remineralized needle-like crystals in the 8DSS-C8-P-113 (MBC) group was less than that in the 8DSS-C8-P-113 (16 μM mL^{-1}) group, with the former exhibiting a layer of plate-like crystals on top (Fig. 3i and j). The observation on Day 7 was similar to that on Day 3, though there was an increase in crystal thickness (Fig. 3o and p). The disparity in outcomes can be attributed to the behaviour of 8DSS-C8-P-113 at different concentrations. At 2 μM mL^{-1}, a thin biofilm formed on the tooth slice surface. Upon immersion in remineralization solutions, 8DSS-C8-P-113 may have quickly dissolved, destabilizing the system. This necessitated daily rebuilding and balancing of the remineralization system, as the coating was applied once and the solution changed daily. Consequently, when the system balance was disrupted, calcium and phosphate tended to aggregate, forming plate-like crystals on the tooth

Table 3
Comparison of properties of peptides.

	Anti-biofouling μM mL^{-1}					Stability	Cyto-compatibility	Promoting remineralization	Inhibiting demineralization in the artificial caries model
	MBC			Anti-adhesion	Anti-biofilm				
	S. mutans	*S. gordonii*	*S. sanguinis*						
C8-P-113	0.03	0.25	0.25	0.25 (8 × MBC)	0.12 (4 × MBC)	–	++	–	+
DPS-C8-P-113	0.25	4.00	2.00	1.00 (4 × MBC)	0.50 (2 × MBC)	++	+	–	++
8DSS-C8-P-113	2.00	32.00	32.00	8.00 (4 × MBC)	16.00 (8 × MBC)	+++	++	MBC: ++ Hydrogel: +++	MBC: +++ Hydrogel: +++

More + represents more effective and - represents ineffective.

surface [45]. In contrast, at 16 μM mL^{-1}, 8DSS-C8-P-113 formed a stable hydrogel net structure on the tooth surface. Even with some dissolution upon immersion, a significant portion of the hydrogel likely remained, maintaining system equilibrium through additional coatings or daily solution changes. It seems that the hydrogel plays a crucial role in stabilizing the remineralization system, enabling calcium and phosphate to orderly pass through the net structure, aggregate, and form needle-like crystals on the tooth surface.

3.4. Artificial caries model

In this study, a closed biofilm model system was used as an artificial caries model [48]. Fig. 4a–f illustrate the cross-section of the lesions on the enamel surface after varied surface treatments. There were higher mineral densities in the outermost layer than that below for all groups. Different lesion depths were shown in Fig. 4g. The mean values of lesion depth in the DPS-C8-P-113 (MBC) (136.09 ± 14.41 μm), 8DSS-C8-P-113 (MBC) (123.74 ± 10.82 μm), and 8DSS-C8-P-113 (16 μM mL^{-1}) (113.57 ± 15.24 μm) groups were significantly lower than that in the control group (154.71 ± 12.92 μm, ***$p < 0.001$). Fig. 4h presented that the mean values of mineral density in the 8DSS-C8-P-113 (MBC) (1.239 ± 0.033 g cm^{-3}), 8DSS-C8-P-113 (16 μM mL^{-1}) (1.311 ± 0.038 g cm^{-3}), and agarose (1.321 ± 0.073 g cm^{-3}) groups were significantly higher than that in the control group (1.125 ± 0.016 g cm^{-3}, ***$p < 0.001$). *S. mutans*, one of the key factors causing dental caries, can metabolize carbohydrates to adhere on the tooth surface and form *S. mutans* biofilm. *S. mutans* can also generate acids from fermentable sugars to acidify the microenvironment [49]. The acid microenvironment causes the demineralization of tooth hard tissues and is an important step in the process of dental caries. Proteins or peptides can inhibit acid production of *S. mutans*. A multi-functional membrane combining lysozyme and polyphemusin I, which adsorbed on the tooth surface, could bind to the HAP to decrease the contact opportunity with acid in one study [50,51]. In another study, a lactotransferrin-derived antimicrobial peptide (LF-1) could suppress the acid production of *S. mutans* by downregulating LDH expression of *S. mutans* at the transcriptional and enzymatic levels [52]. In this study, 8DSS-C8-P-113 (MBC) and 8DSS-C8-P-113 (16 μM mL^{-1}) on the tooth surface showed significant inhibition of demineralization, which might be related to the interaction between peptide and HAP, or the interaction between peptide and *S. mutans*. Furthermore, Matsuda et al. reported that hydrogels containing fluoride could retain on the tooth surface against demineralization; the firmer the consistency of the material, the longer the material remained [53]. The hydrogel status of a material can also provide physical protection, which can be proved by higher mineral density in the agarose group. Both of lesion depth and mineral density are important parameters to evaluate demineralization. Although lesion depth in the agarose group is similar to control group, the mineral density in the agarose group is significantly higher than control group, which may be related to the physical protection from the hydrogel against acid penetration.

Based on the evaluation of above experiments, the comparison of peptide properties is listed in Table 3. 8DSS-C8-P-113 was determined to be the optimal multi-functional AMP, with the specifically targeted anti-*S. mutans* activity, better stability and cytocompatibility, higher ability to improve remineralization and inhibit demineralization in the artificial caries model, and especially self-assembly ability for hydrogel status to promote other properties. To investigate the mechanism of antibacterial activity of 8DSS-C8-P-113, transcriptome analysis of *S. mutans* exposed to 8DSS-C8-P-113 was conducted. To investigate the mechanism of the hydrogel formation of 8DSS-C8-P-113 and the mechanism of improving remineralization of this peptide, MD analysis was applied.

3.5. The mechanism of antibacterial activity of 8DSS-C8-P-113

The effects of 8DSS-C8-P113 at sub-MBC levels on acidogenicity were monitored by the LDH activity of the *S. mutans* culture. The cariogenic virulence factors of *S. mutans*, such as acidogenicity, acid tolerance, and biofilm formation, play a significant role in causing tooth decay [27]. LDH produced by *S. mutans* contributes to acidogenicity by converting pyruvate to lactic acid, which leads to tooth lesions. As shown in Fig. 5a, when *S. mutans* was treated with 8DSS-C8-P113 at 1/4 × MBC and 1/2 × MBC, its LDH activity was significantly lower than that of control group (**$p < 0.01$, ***$p < 0.001$). The absorbance in the groups treated with 8DSS-C8-P113 at 1/4 × MBC and 1/2 × MBC significantly reduced, which indicated that the amount of water-insoluble EPS significantly reduced compared with that in the control group (**$p < 0.01$, ***$p < 0.001$, Fig. 5b). Further analysis of biofilms treated with 8DSS-C8-P113 at 1/8, 1/4 and 1/2 × MBC revealed a thinner, looser biofilm structure with a significantly reduced biomass of bacteria (green) and EPS matrix (red) compared to the untreated control (Fig. 5c). The quantitative analyses of EPS and biofilm formation showed a significant reduction in the amount water-insoluble EPS with 1/8, 1/4 and 1/2 × MBC of 8DSS-C8-P113 (**$p < 0.01$, ***$p < 0.001$, Fig. 5d). EPS produced by bacteria are important components of the biofilm matrix. Various agents have been found to inhibit the activity of *S. mutans* by affecting the production of LDH and EPS. In this study, the treatment group using 8DSS-C8-P113 showed lower levels of LDH and EPS compared to the control group. This suggests that 8DSS-C8-P113 has the ability to reduce acidogenicity and biofilm formation at sub-MBC levels.

To further explore the underlying molecular mechanisms on 8DSS-C8-P-113 reacting to *S. mutans*, the transcriptome analysis of *S. mutans* was performed. Compared with the control group, a total of 238 DEGs were identified in the 8DSS-C8-P-113-treated group ($|\log_2$fold change$| > 1$ and $P < 0.05$), including 158 upregulated genes and 80 downregulated genes (Fig. 5e and Supplementary Table S2). The expression of genes associated with ATP-binding cassette (ABC) transporters (e.g., *RS04395*, *RS04390*, *ugpC*, *msmE*), sugar phosphotransferase system (PTS) (e.g., *lacF*, *RS09600*, *RS05090*), RNA degradation-related genes (*RS03545* and *RS04195*) and lipid metabolism-related genes (e.g., *RS02310*, *RS10100*) were upregulated in the 8DSS-C8-P-113 group (Fig. 5b and Supplementary Table S2). By contrast, DEGs associated

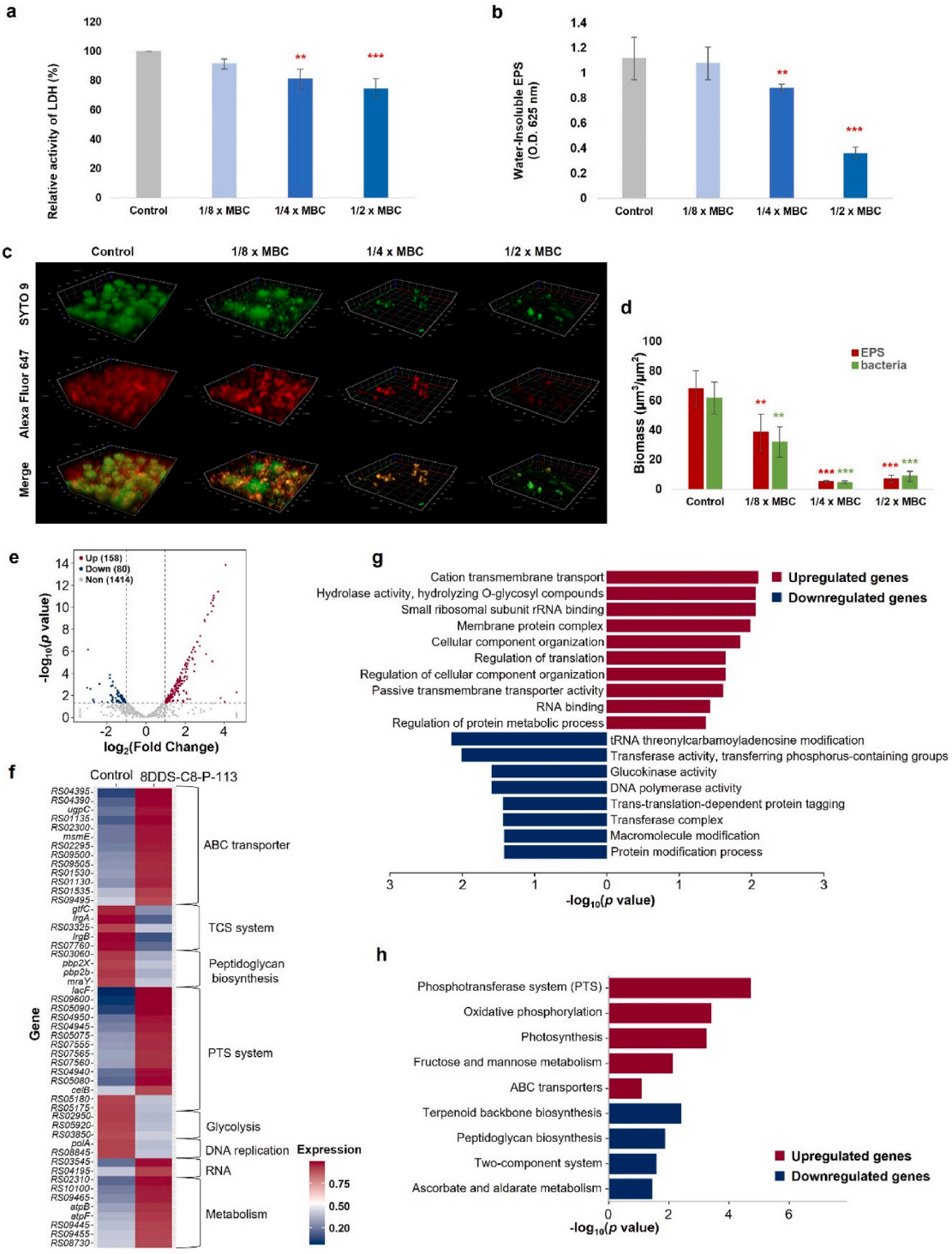

Fig. 5. The mechanism of antibacterial activity of 8DSS-C8-P-113 evaluated by LDH assay, water-insoluble EPS, and transcriptomic analysis of *S. mutans*. (a) LDH activity in the different concentrations of 8DSS-C8-P113 relative to that of the control group. (b) The quantification of water-insoluble EPS of *S. mutans* biofilms in the different concentrations of 8DSS-C8-P113. (c) 3D CLSM image of *S. mutans* (bacteria, stained green; EPS, stained red). (d) Quantitative data of bacterial and EPS biomass in the different concentrations of 8DSS-C8-P113. $*p < 0.05$, $**p < 0.01$, $***p < 0.001$, compared with control group. (e) The volcano plot of DEGs ($|\log_2$fold change$| > 1$ and $P < 0.05$) in *S. mutans* between the control group and 8DSS-C8-P-113-treated group. The abscissa indicates the fold-change in gene expression, while the ordinate indicates significant statistical differences. Red dots represent significantly upregulated genes, blue dots represent significantly downregulated genes, and gray dots represent insignificantly differentially expressed genes. (f) Heatmap of the DEGs between control and 8DSS-C8-P-113-treated group. Red color represents a higher expression level while blue color represents a lower expression level. (g) GO enrichment analysis of the upregulated and downregulated genes between control and 8DSS-C8-P-113-treated group. The x-axis shows the significant statistical differences, and the y-axis indicates the GO terms enriched in the upregulated and downregulated genes. Red and blue indicate the up- and down-regulated genes, respectively. (h) KEGG pathway enrichment analysis of the upregulated and downregulated genes between control and 8DSS-C8-P-113-treated group. The x-axis shows the significant statistical differences, and the y-axis indicates the KEGG pathways enriched in the upregulated and downregulated genes. Red and blue indicate the up- and down-regulated genes, respectively.

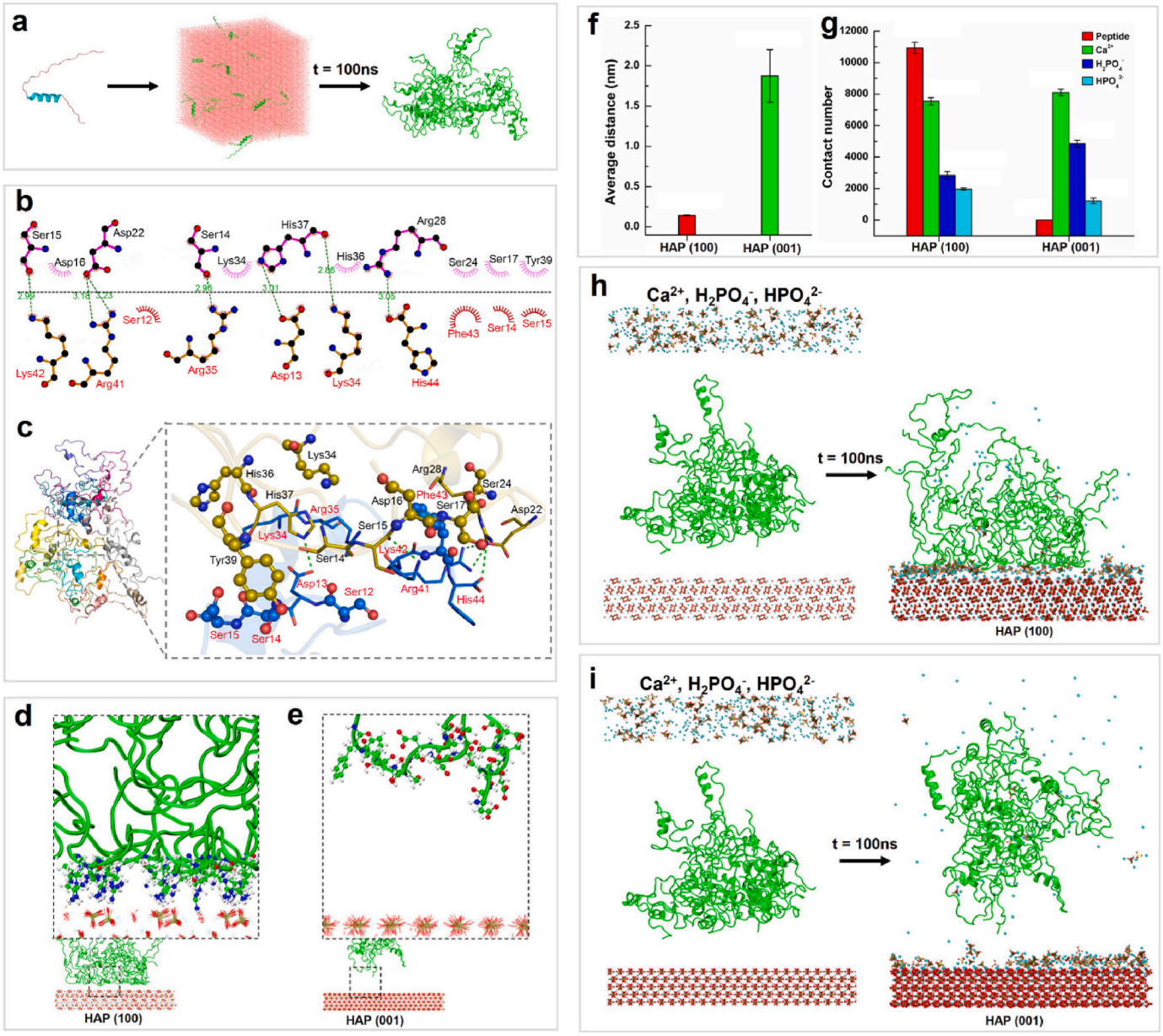

Fig. 6. (a) The structure changes of 8DSS-C8-P-113 in the MD simulation after 100 ns. (b) The 2D binding pattern between two peptides. Green dashed lines represent hydrogen bonding and red gear-shaped structures represent hydrophobic interactions. (c) The 3D binding pattern between two peptides. Green dashed lines represent hydrogen bonding and ball-and-stick models of residues represent hydrophobic interactions. (d) 8DSS-C8-P-113 conformation on the surface of HAP (100). (e) 8DSS-C8-P-113 conformation on the surface of HAP (001). (f) Average distance between 8DSS-C8-P-113 clusters and the surface of HAP. (g) The atomic contact numbers between 8DSS-C8-P-113 hydrogel and HAP surfaces, Ca^{2+} ions and HAP surfaces, $H_2PO_4^-$ and HAP surfaces, and HPO_4^{2-} and HAP surfaces. (h) The adsorption of 8DSS-C8-P-113 hydrogel, Ca^{2+}, $H_2PO_4^-$ and HPO_4^{2-} on the surface of HAP (100) after 100 ns. (i) The adsorption of 8DSS-C8-P-113 hydrogel, Ca^{2+}, $H_2PO_4^-$ and HPO_4^{2-} on the surface of HAP (001) after 100 ns.

with two-component system (TCS) (*gtfC, lrgA, RS03325, lrgB,* and *RS07760*), peptidoglycan biosynthesis (*RS03060, pbp2X, pbp2b,* and *mraY*), glycolysis (*RS02950*, *RS05920*, *RS03850*) and DNA replication (*polA* and *RS04195*) were significantly downregulated in the 8DSS-C8-P-113-treated strain. Notably, the expression of glucan synthesis-related gene *gtfC* was substantially decreased in the 8DSS-C8-P-113 group (Fig. 5f and Supplementary Table S2).

AMPs have broad spectrum antimicrobial activities defencing organisms. The principal antibacterial activities have been attributed to the membrane-lytic and intracellular targeting activities but the details have not been elucidated. For example, antifungal activities to *Candida Albicans* of human peptide Histatin 5 were accredit with multiple intracellular components to induce oxidative stress and mitochondrial malfunction [54]. P-113 killed *S. mutans* by penetrating bacterial membranes and targeting intracellular components such as DNA [17]. These *in vitro* studies show the associations, yet cannot explore unknown or probable mechanisms. Transcriptomic sequencing is a technique that interprets gene function and gene structure, reveal molecular mechanisms of specific biological processes, and discover unknown and rare transcriptional information [55]. Based on the transcriptomic analysis, we provide the probable anti-*S. mutans* mechanism of 8DSS-C8-P-113, including influencing bacterial membranes, inhibiting glycolysis, interfering protein homeostasis and amino acid metabolism, and suppressing DNA replication and oxidation. 8DSS-C8-P-113 may influence the stability or integrity of *S. mutans* bacterial membranes by upregulating PTS system and ABC transporters, and downregulating TCS system and

peptidoglycan biosynthesis of *S. mutans*. S. mutans has a significant number of transporters of the ABC superfamily. Members of this superfamily are involved in the translocation of a diverse range of molecules across the membrane [56]. Some studies showed that ABC transporters and PTS were mainly responsible for the transporting of sugars [57,58]. ABC transporters are well known in increasing the transcription levels for the transportation of sugars, especially under stress conditions. Additionally, they also function in exporting protons to regulate the intracellular pH [58,59]. To survive in the complex oral microenvironment, microorganisms use regulatory networks to detect environmental signals and control adaptive responses. TCS is one of the regulatory networks including QS and antibiotic/bacteriocin production, which typically consists of a membrane associated histidine kinase (VicR) and a cytoplasmic response regulator (VicK) [57,60]. Virulence factors production of *S. mutans* is regulated by TCS genes, including biofilm formation, acidogenicity, aciduricity, genetic transformation and bacteriocin production [61]. Both of VicK and VicR upregulate the expression of GTFC enzyme (one of glucosyltransferase enzymes, GTFs) by binding their promoter regions, and GTFC enzyme is encoded by *gtfC* genes [60]. GTFC enzyme produces a mixture of insoluble and soluble glucans (α-1,6-linked glucose). The insoluble glucans can induce bacterial adhesion on tooth surface and the formation of biofilm, while the soluble glucans can be digested to cause low pH values [62]. In this study, *gtfC* gene was downregulated in the 8DSS-C8-P-113-treated group. The CSP plays a key role in the regulation of bacterial QS. C8, as a CSP in the 8DSS-C8-P-113, may bind with *S. mutans*, activate a transmembrane receptor to interfere the QS of *S. mutans*, and inhibit the function of GTFC enzyme. In the end, 8DSS-C8-P-113 may inhibit *S. mutans*' adhesion, formation of biofilm, and production of acid by downregulating *gtfC* gene. For the inhibition of tooth demineralization in the artificial caries model, it is also a probable and reasonable explanation. The cell wall of most bacteria is made of a large polymer peptidoglycan, which forms a mesh-like scaffold outside the plasma membrane. Peptidoglycan synthesis is crucial for the growth of bacterial cell. Penicillin-binding proteins (PBPs) and transpeptidase catalyse the transglycosylation, transpeptidation, and trimming of the peptidoglycan in the last stage of peptidoglycan biosynthesis [63]. *S. mutans* has five PBPs (PBP1a, PBP1b, PBP2a, PBP2b and PBP2X) which involve in the peptidoglycan biosynthesis [64]. The gene *PBP2X* and *PBP2b* are core-genomes for the class B PBPs, and these PBPs are considered important targets for the beta-lactam antibiotics [65]. In this study, *PBP2X* and *PBP2b* gene were downregulated in the 8DSS-C8-P-113-treated group. 8DSS-C8-P-113 might interfere the peptidoglycan biosynthesis of *S. mutans* to make bacterial cells more prone to osmotic lysis, even to inhibit the growth of *S. mutans*. *S. mutans* is the cariogenic pathogen and synthesize EPS from dietary sugars, which can form plaque biofilm and secrete acids to demineralize teeth. Sugars are the major carbohydrate sources of *S. mutans*. *S. mutans* can use them to produce ATP through glycolysis, to synthesize bacterial components, and to produce polysaccharides and acids [66]. Sugar metabolism is very important for the growth and virulence of *S. mutans*. We found that some genes related to glycolysis were downregulated in the 8DSS-C8-P-113-treated group. 8DSS-C8-P-113 might interfere the glycolysis of *S. mutans* to decrease the virulence of *S. mutans*. The decrease of acid may decline injury to tooth, which may be related to the ability of inhibiting demineralization of 8DSS-C8-P-113.

To further investigate the biological function and potential pathways involved in the antibacterial effect of 8DSS-C8-P-113 on *S. mutans*, the GO and KEGG pathway enrichment analyses were performed, respectively. GO enrichment analysis showed that the upregulated DEGs were enriched in cation transmembrane transport, hydrolase activity, small ribosomal subunit rRNA binding and membrane protein complex, while the downregulated DEGs were enriched in transferase activity, glucokinase activity, DNA polymerase activity and protein modification process (Fig. 5g and Supplementary Table S3, $P < 0.05$). KEGG enrichment analysis indicated that the upregulated DEGs were implicated in PTS system, oxidative phosphorylation and ABC transporters, while the downregulated DEGs were associated with terpenoid backbone biosynthesis, peptidoglycan biosynthesis, TCS system and ascorbate and aldarate metabolism (Fig. 5h and Supplementary Table S4, $P < 0.05$). The results of GO and KEGG pathway enrichment analyses were consistent with the DEGs analyses. Based on the results, we found that 8DSS-C8-P-113 may bind with *S. mutans* and activate a transmembrane receptor to interfere the QS of *S. mutans* by the CSP C8 to inhibit the formation of biofilm, interfere the peptidoglycan biosynthesis of *S. mutans* to cause osmotic lysis, interfere the glycolysis of *S. mutans* to decrease the virulence of *S. mutans*, increase the perforation of cell membrane, and penetrate into the plasm membrane to inhibit DNA polymerase activity and protein modification. Therefore, 8DSS-C8-P-113 inhibits the cariogenic virulence and biological function of *S. mutans* through multiple pathways.

3.6. Mechanism of remineralization

After 100 ns of dynamic simulation, a dispersed state of 20 8DSS-C8-P-113 molecules in a solvent box formed stable clusters of hydrogel nanostructures (Fig. 6a). The formation of a hydrogel from peptide molecules was primarily driven by electrostatic interactions, with an average electrostatic energy of -274210.725 ± 1893.481 kJ mol^{-1} and an average van der Waals energy of -19332.002 ± 2226.747 kJ mol^{-1} (Fig. S4). In the entire system, hydrophobic interactions were the most abundant interactions between peptide molecules, with a mean value of 1135.78. They were followed by hydrogen bonding, with a mean value of 897.10, and pi-pi conjugation interactions were the least prevalent, with a mean value of 64.79 (Fig. S4). The two-dimensional (2D) and 3D binding patterns between two peptides are shown in Fig. 6b and c, respectively. The binding between the two peptide chains was mainly facilitated by hydrogen bonding and hydrophobic interactions. A total of 7 hydrogen bonding interactions were identified between the chains. Asp13, Lys34, Arg35, Arg41, Lys42, and His44 were found to be the primary amino acid residues involved in hydrogen bonding in one peptide chain, while Ser14, Ser15, Asp22, Arg28, and His37 were the main amino acids involved in the other peptide chain. Overall, the analysis results indicate that hydrogen bonding and hydrophobic interactions are the main driving forces behind the aggregation of dispersed peptide molecules into a hydrogel in the entire system, with electrostatic interactions playing a promotional role. Additionally, the hydrogen bonding and hydrophobic interactions between charged amino acid residues, such as serine, aspartic acid, lysine, arginine, and histidine, play a crucial role in this process. From a functional perspective, hydrogen bonding interactions predominantly occur between functional groups that carry either a partial or a full charge.

It can be observed in Fig. 6d that 8DSS-C8-P-113 hydrogel moved towards the HAP (100) surface and was stably adsorbed through hydrogen bonding interactions between the side chain amino groups of lysine and arginine amino acids in the hydrogel and HAP. However, weak interactions between the 8DSS-C8-P-113 hydrogel and the HAP (001) surface prevented the entire peptide cluster from adsorbing onto the surface and exhibiting obvious interactions (Fig. 6e). During the entire simulation process, the average distance between the hydrogel and the HAP (100) surface (0.144 ± 0.006 nm) was shorter than that between the hydrogel and the HAP (001) surface (1.875 ± 0.327 nm) (Fig. 6f). It is observed that the HAP (100) surface exhibits a stronger affinity for the 8DSS-C8-P-113 hydrogel through hydrogen bonding, while the HAP (001) surface has a weaker affinity.

In the system, the contact number between the hydrogel ions and HAP (100) surface was significantly higher than that with the HAP (001) surface (Fig. 6g). The contact number of the free HPO_4^{2-} phosphate ions on the HAP (100) surface was slightly higher than that on the HAP (001) surface. However, the contact number of the free Ca^{2+} ions on the HAP (100) surface was lower than that on the HAP (001) surface, which was consistent with the radial distribution results (Fig. S5). The contact

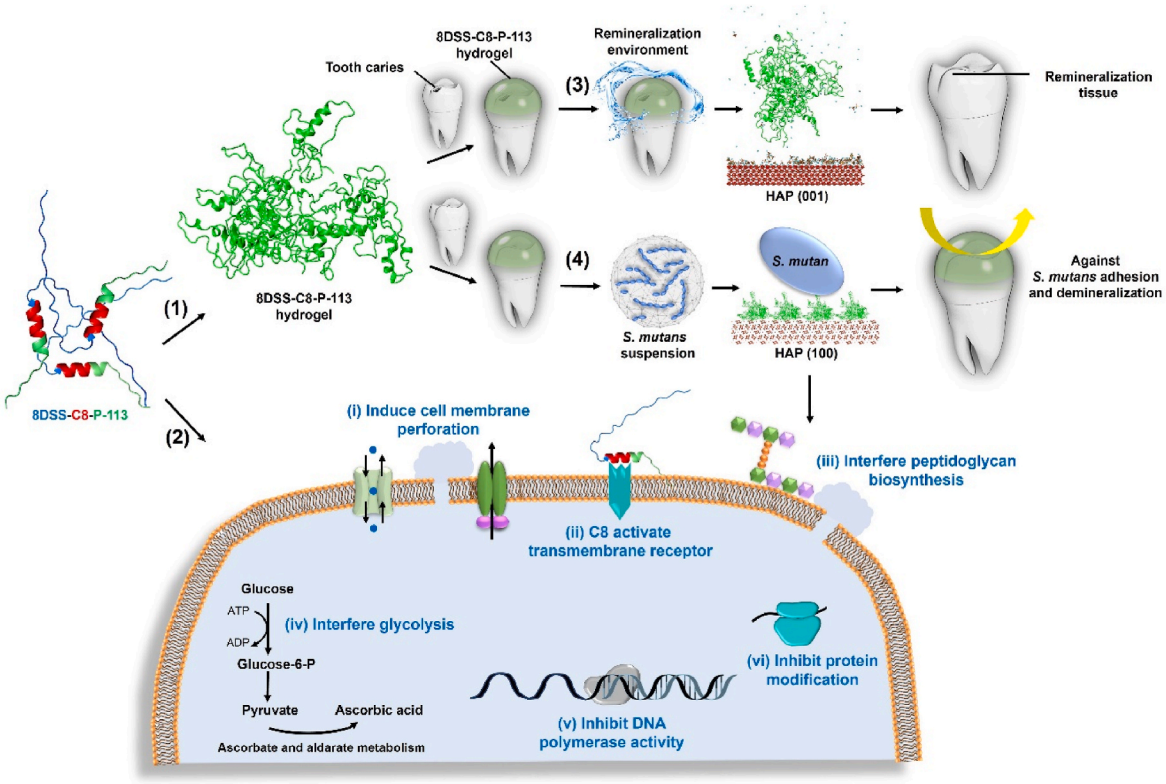

Fig. 7. Schematic diagram illustrating the functions of 8DSS-C8-P-113. (1) 8DSS-C8-P-113 molecules form a hydrogel state and adhere to the tooth surface. The molecule structure consists of a blue part representing 8DSS, a red part representing C8, and a green part representing P-113. (2) Potential antibacterial mechanism of 8DSS-C8-P-113 on *S. mutans* is as follows: (i) inducing cell membrane perforation, (ii) C8 activating a transmembrane receptor and interfering with QS, (iii) interfering with peptidoglycan biosynthesis, (iv) interfering with glycolysis, (v) inhibiting DNA polymerase activity, and (vi) inhibiting protein modification. (3) 8DSS-C8-P-113 hydrogel induces Ca^{2+}, $H_2PO_4^-$, and HPO_4^{2-} adhering to HAP (001), forming a remineralization layer. (4) 8DSS-C8-P-113 hydrogel adsorbs on HAP (100), inhibits *S. mutans*' adhesion, and reduces tooth demineralization.

number of the free $H_2PO_4^-$ ions on the HAP (100) surface was also lower than that of the HAP (001) surface. Fig. 6h showed that Ca^{2+}, $H_2PO_4^-$, and HPO_4^{2-} ions were randomly dispersed in a rectangular area 2 nm above 8DSS-C8-P-113 hydrogel in the HAP (100) system before simulation. After 100 ns, the hydrogel adsorbed onto the HAP (100) surface, causing the clusters to become looser. Due to the adsorption of 8DSS-C8-P-113 hydrogel molecules, most of the HAP (100) surface area was occupied by the hydrogel molecules, while Ca^{2+}, $H_2PO_4^-$, and HPO_4^{2-} ions were relatively more concentrated in areas uncovered by peptides. In Fig. 6i, most of Ca^{2+}, $H_2PO_4^-$, and HPO_4^{2-} ions adsorbed onto the HAP (001) surface and were more dispersedly and evenly distributed, while the 8DSS-C8-P-113 hydrogel molecules did not adsorb onto the HAP (001) surface after 100 ns of MD simulation. The difference in the adsorption of 8DSS-C8-P-113 hydrogel on the two HAP surfaces affects the adsorption between the ions and HAP surface. Ca^{2+} and $H_2PO_4^-$ ions are found to aggregate less on the HAP (100) surface. This may due to the adsorption of the 8DSS-C8-P-113 hydrogel occupying most of the surface area of HAP (100), thereby suppressing the adsorption of ions to some extent. HPO_4^{2-} ions also aggregates less on the HAP (001) surface, possibly because more $H_2PO_4^-$ phosphate ions occupy most of the space on the HAP (001) surface. Therefore, the molecular simulation results indicate that the 8DSS-C8-P-113 hydrogel exhibits minimal adsorption on the HAP (001) surface. As there is no spatial hindrance from the 8DSS-C8-P-113 hydrogel on the HAP (001) surface, calcium and phosphate ions are more likely to aggregate on the surface, leading to the growth of the crystal structure along the (001) direction.

Needle-like remineralization crystals form along the HAP (001) direction [67]. In Fig. 3d–j, p, it is illustrated that the 8DSS-C8-P-113 hydrogel applied on tooth surface prompts the development of needle-like remineralization crystals on top of tooth surface, yet beneath the hydrogel. Consequently, upon application of the 8DSS-C8-P-113 hydrogel, only the HAP (001) surface remains accessible for calcium and phosphate ions. Functioning as a template, the 8DSS-C8-P-113 hydrogel effectively guides the formation of new crystals along the HAP (001) direction. Although there is a possibility that part of the hydrogel may dissolve in saliva, a portion of it persists on the tooth surface, attracting calcium and phosphate ions. By maintaining a stable environment and safeguarding these ions, the remaining hydrogel aids in the aggregation of ions on the tooth surface, steering them towards remineralization along the HAP (001) direction.

3.7. Schema of mechanism

Based on the results in this study, the multiple functions of 8DSS-C8-P-113 is illustrated in Fig. 7 and its hypothesized bioactivities are summarized as follows. Firstly, numerous of 8DSS-C8-P-113 molecules self-assemble a hydrogel state and adhere to the tooth surface. Secondly, 8DSS-C8-P-113 kills planktonic *S. mutans*, inhibits *S. mutans*' adhesion, eradicates *S. mutans*' biofilm, and reduces *S. mutans*' virulence. The probable mechanisms of 8DSS-C8-P-113 interfering *S. mutans* include: 1) It induces cell membrane perforation by up-regulating cation transmembrane transport and ABC-transporter. 2) C8 in 8DSS-C8-P-113 activates a transmembrane receptor, leading to interference with QS and inhibition of biofilm formation by down-regulation of TCS. 3) It interferes with peptidoglycan biosynthesis, resulting in osmotic lysis. 4) It interferes with glycolysis, causing decreased virulence by down-regulating glucokinase activity, as well as ascorbate and aldarate metabolism. 5) 8DSS-C8-P-113 inhibits DNA polymerase activity. 6) 8DSS-C8-P-113 inhibits protein modification. Thirdly, when exposed to the remineralization solution, 8DSS-C8-P-113 hydrogel on the enamel

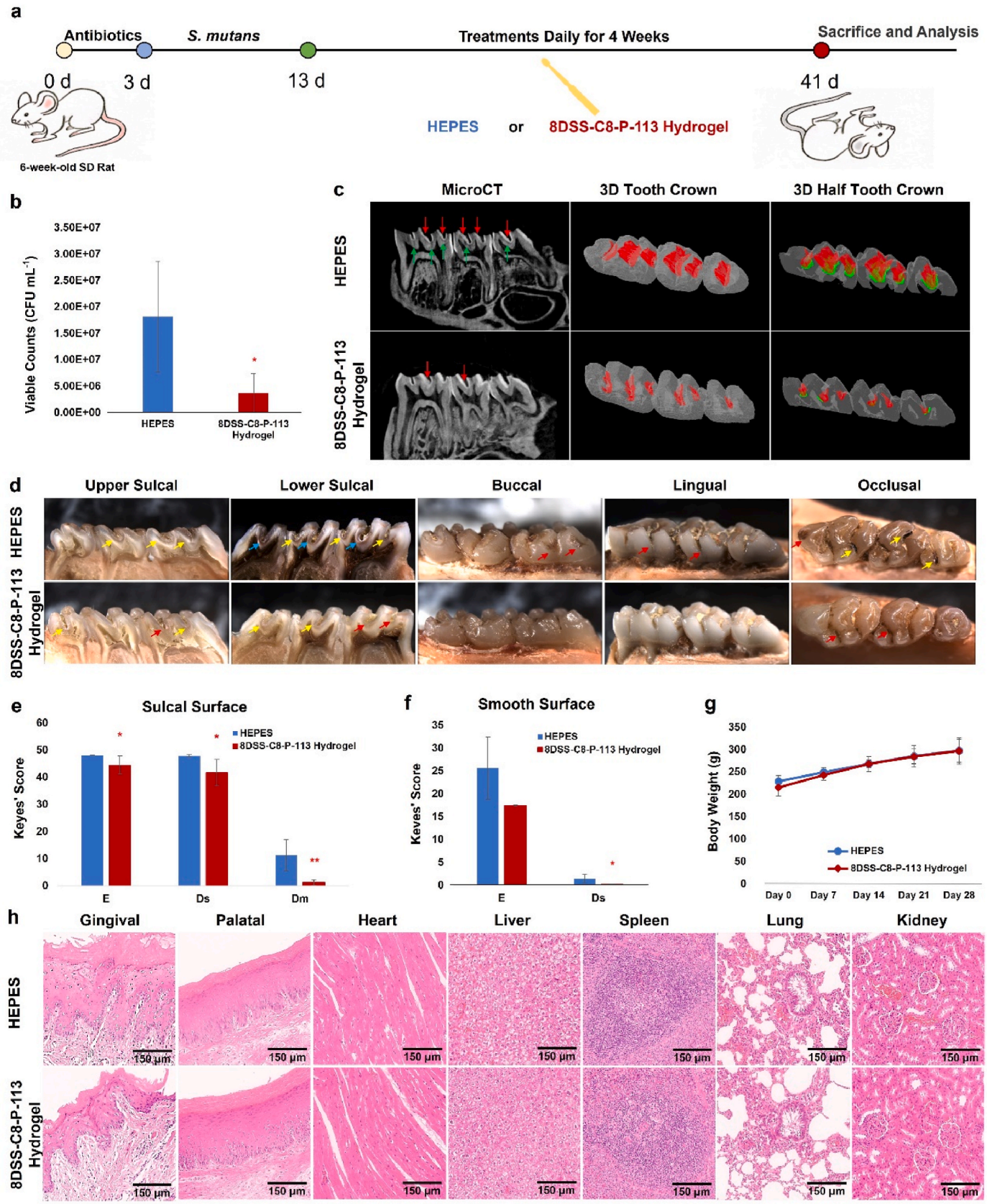

Fig. 8. Evaluation of caries prevention in a rat dental caries model. (a) Schematic diagram of the in vivo experimental procedure. (b) Quantification of *S. mutans* CFU in each group. (c) MicroCT images (Red arrow: Enamel lesions; Green arrow: Dentin lesions) and 3D reconstruction images of rat teeth (Enamel lesions in red; Dentin lesions in green). (d) Stereomicroscope images of the sulcal surface, buccal surface, lingual surface, and occlusal surface (Red arrow: E; Yellow arrow: Ds; Blue arrow: Dm). (e) Keyes' score of the sulcal surface. (f) Keyes' score of the smooth surface. (g) Body weights of rats. (h) Histopathology of rat tissues from gingiva, palate, heart, liver, spleen, lung, and kidney. $^{*}p < 0.05$, $^{**}p < 0.01$, compared with HEPES group.

surface induces the adherence of essential ions, including Ca^{2+}, $H_2PO_4^-$, and HPO_4^{2-}, to HAP (001). This process facilitates the formation of a needle-shaped remineralization crystal layer between the 8DSS-C8-P-113 hydrogel and the tooth surface. Fourthly, 8DSS-C8-P-113 hydrogel adsorbs onto the HAP (100) surface, effectively inhibiting the adhesion of *S. mutans* and subsequently reducing tooth demineralization.

The specific targeting agent 8DSS-C8-P-113, at a concentration of 2 μM mL^{-1}, can be used as a mouthwash for personal care at home to effectively eliminate planktonic *S. mutans* without disrupting the oral normal flora, such as *S. gordonii* and *S. sanguinis*. For professional care at dental clinic, 8DSS-C8-P-113 with the concentration of 8 μM mL^{-1} can be employed in the form of varnish to prevent *S. mutans'* adhesion. The hydrogel formed from 8DSS-C8-P-113 with the concentration of 16 μM mL^{-1} can be applied directly to eradicate *S. mutans'* biofilm, safeguard teeth against acid injury, and facilitate the repair of demineralized hard tissue.

3.8. Suppression of dental caries in a rat caries model

The preventive efficacy of 8DSS-C8-P-113 for dental caries in vivo was determined using a rat dental caries model. The experimental procedure for the rat dental caries model is shown in Fig. 8a. Compared to the control group treated with HEPES only, rats treated with 8DSS-C8-P-113 presented a significant decrease in *S. mutans* CFU from dental plaques ($P < 0.05$) (Fig. 8b). Fig. 8c shows MicroCT images, 3D reconstruction images of the complete tooth crown, and 3D reconstruction images of half tooth crown. Compared to the HEPES group, the volume of enamel lesions (red) and dentin lesions (green) on rat teeth was reduced in the 8DSS-C8-P-113 group. As shown in Fig. 8d, enamel and dentin lesions were more severe in the HEPES group. Enamel caries (red arrow) was observed on the buccal, lingual, and proximal surfaces, and the lesions on the sulcal surface were deeper than half dentin thickness (blue arrow). On the sulcal surface, the Keyes' scores were significantly lower in the 8DSS-C8-P-113 group than in the HEPES group (E and Ds: $P < 0.05$, Dm: $P < 0.01$) (Fig. 8e). On the smooth surface, the Keyes' scores of Ds were significantly lower in the 8DSS-C8-P-113 group than in the HEPES group (Ds: $P < 0.05$) (Fig. 8f). All rats survived without significant differences in body weights observed between HEPES and 8DSS-C8-P-113 groups (Fig. 8g). No signs of inflammatory reaction, proliferative changes, or necrosis were observed in the histopathology analysis of both groups (Fig. 8h). These results demonstrate that 8DSS-C8-P-113 can effectively reduce the severity of caries in the rat caries model. Along with its good biocompatibility, it can be a potent and safe agent for clinical application in humans. It is important to acknowledge the limitations of this study, which include the absence of mechanical property data for 8DSS-C8-P-113 and the lack of in vivo investigations on its remineralization ability. The concentration of 16 μM mL^{-1} was selected in the rat caries model specifically to evaluate the biocompatibility of 8DSS-C8-P-113 at a higher concentration. Additionally, while the experiment showed a reduction in caries severity in the treatment group, there were still instances of dental caries in the extremely cariogenic environment, which may also have been due to operational difficulties in the small rat mouth. Therefore, further investigations are necessary to explore the various factors that may influence the efficacy of 8DSS-C8-P-113 and to address the limitations of this study.

4. Conclusions

The multi-functional agent 8DSS-C8-P-113 is designed for targeted elimination of *S. mutans* while preserving beneficial bacteria like *S. gordonii* and *S. sanguinis*. At a concentration of 2 μM mL^{-1}, it effectively kills *S. mutans*, activating a transmembrane receptor that disrupts cell membranes, inhibits peptidoglycan biosynthesis, and reduces DNA polymerase activity. At 8 μM mL^{-1}, it prevents *S. mutans* adhesion by interfering with glycolysis, while at 16 μM mL^{-1}, it eradicates *S. mutans* biofilm by disrupting quorum sensing and inhibiting extracellular polymeric substance production. Additionally, it suppresses demineralization by inhibiting LDH production and forming a protective hydrogel on tooth surfaces, facilitating remineralization through calcium and phosphate ion binding. In a rat caries model, 8DSS-C8-P-113 demonstrates practical efficacy and safety, indicating its potential as a therapeutic agent for preventing and treating dental caries.

CRediT authorship contribution statement

Li Zhou: Writing – original draft, Validation, Methodology, Formal analysis, Data curation. **Qing Liu:** Writing – review & editing, Software, Methodology. **Zehui Fang:** Methodology. **Quan Li Li:** Writing – review & editing, Project administration, Funding acquisition, Conceptualization. **Hai Ming Wong:** Writing – review & editing, Supervision, Project administration, Funding acquisition, Data curation, Conceptualization.

Ethics approval and consent to participate

Human third molars were obtained from patients who provided written informed consent, and the study was approved by the Institutional Review Board of the University of Hong Kong/Hospital Authority Hong Kong West Cluster (IRB No: UW22-657). Human saliva was collected from a volunteer who provided written informed consent, which was approved by the Institutional Review Board of the University of Hong Kong/Hospital Authority Hong Kong West Cluster (IRB No: UW22-657). All animal-related operations in this work were approved by the Ethics Committee of Anhui Medical University, China (ref. no. LLSC20232002).

Declaration of competing interest

The authors declare no conflict of interest.

Acknowledgements

The work described in this paper was fully supported by a grant from the NSFC/RGC Joint Research Scheme sponsored by the Research Grants Council of the Hong Kong Special Administrative Region, China and the National Natural Science Foundation of China (Project No. N_HKU706/20 and No. 82061160492). Human third molars were obtained from patients who provided written informed consent, and the study was approved by the Institutional Review Board of the University of Hong Kong/Hospital Authority Hong Kong West Cluster (IRB No: UW22-657). Human saliva was collected from a volunteer who provided written informed consent, which was approved by the Institutional Review Board of the University of Hong Kong/Hospital Authority Hong Kong West Cluster (IRB No: UW22-657). All animal-related operations in this work were approved by the Ethics Committee of Anhui Medical University, China (ref. no. LLSC20232002).

Appendix A. Supplementary data

Supplementary data to this article can be found online at https://doi.org/10.1016/j.bioactmat.2024.10.022.

References

[1] D.F. Pancu, A. Scurtu, I.G. Macasoi, D. Marti, M. Mioc, C. Soica, D. Coricovac, D. Horhat, M. Poenaru, C. Dehelean, Antibiotics: conventional therapy and natural compounds with antibacterial activity-a pharmaco-toxicological screening, Antibiotics 10 (2021) 401.

[2] J.R. Namburu, A.B. Rajendra Sanosh, C.S. Poosarla, S. Manthapuri, M. Pinnaka, V. R. Reddy Baddam, Streptococcus mutans-specific antimicrobial peptide C16G2-mediated caries prevention: a review, Front. Dent. 19 (2022) 17.

[3] S. Mai, M.T. Mauger, L.N. Niu, J.B. Barnes, S. Kao, B.E. Bergeron, J.Q. Ling, F. R. Tay, Potential applications of antimicrobial peptides and their mimics in combating caries and pulpal infections, Acta Biomater. 49 (2017) 16–35.

[4] Y. Huan, Q. Kong, H. Mou, H. Yi, Antimicrobial peptides: classification, design, application and research progress in multiple fields, Front. Microbiol. 11 (2020) 582779.
[5] J.Y. Niu, I.X. Yin, M.L. Mei, W.K.K. Wu, Q.L. Li, C.H. Chu, The multifaceted roles of antimicrobial peptides in oral diseases, Mol. Oral Microbiol. 36 (3) (2021) 159–171.
[6] M. Erdem Büyükkiraz, Z. Kesmen, Antimicrobial peptides (AMPs): a promising class of antimicrobial compounds, J. Appl. Microbiol. 132 (2022) 1573–1596.
[7] P. Sarma, S. Mahendiratta, A. Prakash, B. Medhi, Specifically targeted antimicrobial peptides: a new and promising avenue in selective antimicrobial therapy, Indian J. Pharmacol. 50 (2018) 1–3.
[8] K. Tang, X. Wang, M. Niu, X. Wang, G. Zhou, J. Shi, Y. Yu, Z. Chen, C. Li, Augmenting the precise targeting of antimicrobial peptides (AMPs) and AMP-based drug delivery via affinity-filtering strategy, Adv. Funct. Mater. 32 (2022) 2111344.
[9] K. Yadav, S. Prakash, Dental caries: a microbiological approach, Infect. Dis. Clin. Pract. 2 (2017) 118.
[10] S.D. Forssten, M. Bjorklund, A.C. Ouwehand, Streptococcus mutans, caries and simulation models, Nutrients 2 (2010) 290–298.
[11] J.Y. Niu, I.X. Yin, W.K.K. Wu, Q.L. Li, M.L. Mei, C.H. Chu, Antimicrobial peptides for the prevention and treatment of dental caries: a concise review, Arch. Oral Biol. 122 (2021) 105022.
[12] K. Ouhara, H. Komatsuzawa, S. Yamada, H. Shiba, T. Fujiwara, M. Ohara, K. Sayama, K. Hashimoto, H. Kurihara, M. Sugai, Susceptibilities of periodontopathogenic and cariogenic bacteria to antibacterial peptides, β-defensins and LL37, produced by human epithelial cells, J. Antimicrob. Chemother. 55 (2005) 888–896.
[13] R. Eckert, J. He, D.K. Yarbrough, F. Qi, M.H. Anderson, W. Shi, Targeted killing of Streptococcus mutans by a pheromone-guided "smart" antimicrobial peptide, Antimicrob, Agents Chemother 50 (2006) 3651–3657.
[14] K.T. Cheng, C.L. Wu, B.S. Yip, Y.H. Chih, K.L. Peng, S.Y. Hsu, H.Y. Yu, J.W. Cheng, The interactions between the antimicrobial peptide P-113 and living Candida albicans cells shed light on mechanisms of antifungal activity and resistance, Int. J. Mol. Sci. 21 (2020) 2654.
[15] H.P. Stallmann, C. Faber, A.L.J.J. Bronckers, J.M.A. de Blieck-Hogervorst, C.P.J. M. Brouwer, A.V.N. Amerongen, P.I.J.M. Wuisman, Histatin and lactoferrin derived peptides: antimicrobial properties and effects on mammalian cells, Peptides 26 (2005) 2355–2359.
[16] D.M. Rothstein, P. Spacciapoli, L.T. Tran, T. Xu, F.D. Roberts, M. Dalla Serra, D. K. Buxton, F.G. Oppenheim, P. Friden, Anticandida activity is retained in P-113, a 12-amino-acid fragment of Histatin 5, Antimicrob. Agents Chemother. 45 (2001) 1367–1373.
[17] L. Huo, K. Zhang, J. Ling, Z. Peng, X. Huang, H. Liu, L. Gu, Antimicrobial and DNA-binding activities of the peptide fragments of human lactoferrin and histatin 5 against Streptococcus mutans, Arch. Oral Biol. 56 (2011) 869–876.
[18] L. Zhou, Q.L. Li, H.M. Wong, A novel strategy for caries management: constructing an antibiofouling and mineralizing dual-bioactive tooth surface, ACS Appl. Mater. Interfaces 13 (2021) 31140–31152.
[19] W. Zheng, L. Ding, Y. Wang, S. Han, S. Zheng, Q. Guo, W. Li, X. Zhou, L. Zhang, The effects of 8DSS peptide on remineralization in a rat model of enamel caries evaluated by two nondestructive techniques, J Appl Biomater Func 17 (2019) 2280800019827798.
[20] L. Zhang, Z. Fang, Q.L. Li, C.Y. Cao, A tooth-binding antimicrobial peptide to prevent the formation of dental biofilm, Journal of materials science, J. Mater. Sci. Mater. Med. 30 (2019) 45–49.
[21] G.X. Wei, A.N. Campagna, L.A. Bobek, Effect of MUC7 peptides on the growth of bacteria and on Streptococcus mutans biofilm, J. Antimicrob. Chemother. 57 (2006) 1100–1109.
[22] L. Zhou, H.M. Wong, Y.Y. Zhang, Q.L. Li, Constructing an antibiofouling and mineralizing bioactive tooth surface to protect against decay and promote self-healing, ACS Appl. Mater. Interfaces 12 (2020) 3021–3031.
[23] Z. Huang, X. Shi, J. Mao, S. Gong, Design of a hydroxyapatitebinding antimicrobial peptide with improved retention and antibacterial efcacy for oral pathogen control, Sci. Rep. 6 (2016) 38410.
[24] Y. Cao, M.L. Mei, Q.L. Li, E.C.M. Lo, C.H. Chu, Agarose hydrogel biomimetic mineralization model for the regeneration of enamel prismlike tissue, ACS Appl. Mater. Interfaces 6 (2014) 410–420.
[25] Y.Z. Zhou, Y. Cao, W. Liu, Q.L. Li, C.H. Chu, Polydopamine-induced tooth remineralization, ACS Appl. Mater. Interfaces 4 (2012) 6901–6910.
[26] H. Koo, M.F. Hayacibara, B.D. Schobel, J.A. Cury, P.L. Rosalen, Y.K. Park, A. M. Vacca-Smith, W.H. Bowen, Inhibition of Streptococcus mutans biofilm accumulation and polysaccharide production by apigenin and tt-farnesol, J. Antimicrob. Chemother. 52 (2003) 782–789.
[27] Y. Wang, X. Wang, W. Jiang, K. Wang, J. Luo, W. Li, X. Zhou, L. Zhang, Antimicrobial peptide GH12 suppresses cariogenic virulence factors of Streptococcus mutans, J. Oral Microbiol. 10 (2018) 1442089–14420811.
[28] J. Jumper, R. Evans, A. Pritzel, T. Green, M. Figurnov, O. Ronneberger, K. Tunyasuvunakool, R. Bates, A. Žídek, A. Potapenko, A. Bridgland, C. Meyer, S.A. A. Kohl, A.J. Ballard, A. Cowie, B. Romera-Paredes, S. Nikolov, R. Jain, J. Adler, T. Back, S. Petersen, D. Reiman, E. Clancy, M. Zielinski, M. Steinegger, M. Pacholska, T. Berghammer, S. Bodenstein, D. Silver, O. Vinyals, A.W. Senior, K. Kavukcuoglu, P. Kohli, D. Hassabis, Highly accurate protein structure prediction with AlphaFold, Nature 596 (2021) 583–589.
[29] Y. Lin, T. Gong, Q. Ma, M. Jing, T. Zheng, J. Yan, J. Chen, Y. Pan, Q. Sun, X. Zhou, Y. Li, Nicotinamide could reduce growth and cariogenic virulence of Streptococcus mutans, J. Oral Microbiol. 14 (2022) 2056291.
[30] P.H. Keyes, Dental caries in the molar teeth of rats: II. a method for diagnosing and scoring several types of lesions simultaneously, J. Dent. Res. 37 (1958) 1088–1099.
[31] Q. Li, J. Liu, H. Liu, Y. Sun, Y. Xu, K. Wang, W. Huang, L. Liao, X. Wang, Multifunctional magnesium organic framework-based photothermal and pH dual-responsive mouthguard for caries prevention and tooth self-healing promotion, Bioact. Mater. 29 (2023) 72–84.
[32] D. Liu, X. Ma, Y. Ji, R. Chen, S. Zhou, H. Yao, Z. Zhang, M. Ye, Z. Xu, M. Du, Bioresponsive nanotherapy for preventing dental caries by inhibiting multispecies cariogenic biofilms, Bioact. Mater. 14 (2022) 1–14.
[33] L. Huo, X. Huang, J. Ling, H. Liu, J. Liu, Selective activities of STAMPs against Streptococcus mutans, Exp. Ther. Med. 15 (2018) 1886–1893.
[34] R.T. Syvitski, X.L. Tian, K. Sampara, A. Salman, S.F. Lee, D.L. Jakeman, Y.H. Li, Structure-activity analysis of quorum-sensing signaling peptides from Streptococcus mutans, J. Bacteriol. 189 (2007) 1441–1450.
[35] L. Zhou, H.M. Wong, Q.L. Li, Anti-biofouling coatings on the tooth surface and hydroxyapatite, Int. J. Nanomed. 15 (2020) 8963–8982.
[36] S.H. Aswathy, U. Narendrakumar, I. Manjubala, Commercial hydrogels for biomedical applications, Heliyon 6 (2020) e03719.
[37] G.B. Qi, Y.J. Gao, L. Wang, H. Wang, Self-assembled peptide-based nanomaterials for biomedical imaging and therapy, Adv. Mater. 30 (2018) e1703444.
[38] M. Bahram, N. Mohseni, M. Moghtader, An Introduction to Hydrogels and Some Recent Applications, IntechOpen, 2016.
[39] C.F. Guimarães, R. Ahmed, A.P. Marques, R.L. Reis, U. Demirci, Engineering hydrogel-based biomedical photonics: design, fabrication, and applications, Adv. Mater. 33 (2021) e2006582.
[40] S. Liu, W. Guo, Anti-biofouling and healable materials: preparation, mechanisms, and biomedical applications, Adv. Funct. Mater. 28 (2018) 1800596.
[41] A.H. Sakr, M.S. Nassif, D.I. El-Korashy, Amelogenin-inspired peptide, calcium phosphate solution, fluoride and their synergistic effect on enamel biomimetic remineralization: an in vitro pH-cycling model, BMC Oral Health 24 (2024) 279.
[42] J. Inukai, A. Yanagida, S. Tsuruta, S. Takeichi, T. Kosakal, De and remineralization cycles and fluoride effect on microhardness and roughness of enamel surface, Dent Oral Craniofac Res 3 (2017) 1–4.
[43] P. DenBesten, W. Li, Chronic fluoride toxicity: dental fluorosis, Monogr. Oral Sci. 22 (2011) 81–96.
[44] Y. Fan, Z. Sun, J. Moradian-Oldak, Effect of fluoride on the morphology of calcium phosphate crystals grown on acid-etched human enamel, Caries Res. 43 (2009) 132–136.
[45] A. Ruffini, S. Sprio, L. Preti, A. Tampieri, Synthesis of nanostructured hydroxyapatite via controlled hydrothermal route, in: M. Barbeck, O. Jung, R. Smeets, T. Korzinskas (Eds.), Biomaterial-supported Tissue Reconstruction or Regeneration, 2019. IntechOpen.
[46] H.M. Wong, Y.Y. Zhang, Q.L. Li, An enamel-inspired bioactive material with multiscale structure and antibacterial adhesion property, Bioact. Mater. 7 (2022) 491–503.
[47] C. Li, D. Lu, J. Deng, X. Zhang, P. Yang, Amyloid-like rapid surface modification for antifouling and in-depth remineralization of dentine tubules to treat dental hypersensitivity, Adv. Mater. 31 (2019) 1903973.
[48] O.Y. Yu, I.S. Zhao, M.L. Mei, E.C.M. Lo, C.H. Chu, A review of the common models used in mechanistic studies on demineralization-remineralization for cariology research, Dent. J. 5 (2017) 20.
[49] W.H. Bowen, H. Koo, Biology of Streptococcus mutans-derived glucosyltransferases: role in extracellular matrix formation of cariogenic biofilms, Caries Res. 45 (2011) 69–86.
[50] Z. Fang, Y. Zhang, C.Y. Cao, Q.L. Li, H.M. Wong, Constructing an anti-*S. mutans* and mineralizing membrane by combination self-assembled lysozyme with antimicrobial peptide, Mater. Des. 220 (2022) 110891.
[51] D. Wang, J. Deng, X. Deng, C. Fang, X. Zhang, P. Yang, Controlling enamel remineralization by amyloid-like amelogenin mimics, Adv. Mater. 32 (2020) e2002080.
[52] J. Luo, Z. Feng, X. Lyu, L. Zhang, Novel lactotransferrin-derived antimicrobial peptide LF-1 inhibits the cariogenic virulence factors of Streptococcus mutans, Antibiotics 12 (2023) 563.
[53] Y. Matsuda, B. Altankhishig, K. Okuyama, H. Yamamoto, K. Naito, M. Hayashi, H. Sano, S.K. Sidhu, T. Saito, Inhibition of demineralization of dentin by fluoride-containing hydrogel desensitizers: an in vitro study, J. Funct. Biomater. 13 (2022) 246.
[54] S. Puri, M. Edgerton, How does it kill?: understanding the candidacidal mechanism of salivary histatin 5, Eukaryot. Cell 13 (2014) 958–964.
[55] X. Yang, L. Kui, M. Tang, D. Li, K. Wei, W. Chen, J. Miao, Y. Dong, High-throughput transcriptome profiling in drug and biomarker discovery, Front. Genet. 11 (2020) 19.
[56] A.J. Webb, A.H.F. Hosie, A member of the second carbohydrate uptake subfamily of ATP-binding cassette transporters is responsible for ribonucleoside uptake in Streptococcus mutans, J. Bacteriol. 188 (2006) 8005–8012.
[57] J. Kong, K. Xia, X. Su, X. Zheng, C. Diao, X. Yang, X. Zuo, J. Xu, X. Liang, Mechanistic insights into the inhibitory effect of theaflavins on virulence factors production in Streptococcus mutans, Amb. Express 11 (2021) 102.
[58] S.S.A. Mubarak, Systematic Analysis of ABC Transporters in Streptococcus Sanguinis, Virginia Commonwealth University, Master Thesis, 2013, p. 89.
[59] D. Ajdic, V.T.T. Pham, Global transcriptional analysis of Streptococcus mutans sugar transporters using microarrays, J. Bacteriol. 189 (2007) 5049–5059.
[60] Q. Zhang, Q. Ma, Y. Wang, H. Wu, J. Zou, Molecular mechanisms of inhibiting glucosyltransferases for biofilm formation in Streptococcus mutans, Int. J. Oral Sci. 13 (2021) 30.

[61] K. Shanmugam, H.B. Sarveswari, A. Udayashankar, S.S. Swamy, A. Pudipeddi, T. Shanmugam, A.P. Solomon, P. Neelakantan, Guardian genes ensuring subsistence of oral Streptococcus mutans, Crit. Rev. Microbiol. 46 (2020) 475–491.
[62] R.A. Burne, Y.Y. Chen, J.E. Penders, Analysis of gene expression in Streptococcus mutans in biofilms in vitro, Adv. Dent. Res. 11 (1997) 100–109.
[63] J.L. Mainardi, M. Fourgeaud, J.E. Hugonnet, L. Dubost, J.P. Brouard, J. Ouazzani, L.B. Rice, L. Gutmann, M. Arthur, A novel peptidoglycan cross-linking enzyme for a β-lactam-resistant transpeptidation pathway, J. Biol. Chem. 280 (2005) 38146–38152.
[64] S.N. Park, S.J. Ahn, J.K. Kook, Oleanolic acid and ursolic acid inhibit peptidoglycan biosynthesis in Streptococcus mutans UA159, Braz. J. Microbiol. 46 (2015) 613–617.
[65] B.D. Pangabam, R.S. Naorem, A.B. Teli, C. Fekete, Immunoinformatics-driven multiepitope vaccine targeting Streptococcus mutans for dental caries prevention, Res. Sq. (2023).
[66] M. Kawada-Matsuo, Y. Oogai, H. Komatsuzawa, Sugar allocation to metabolic pathways is tightly regulated and affects the virulence of Streptococcus mutans, Genes 8 (2016) 11.
[67] W. Wang, Z. Xu, R. Wang, X. Wang, D. Xu, Molecular dynamics exploration of the growth mechanism of hydroxyapatite nanoparticles regulated by glutamic acid, J. Phys. Chem. B 125 (2021) 5078–5088.